Examining Terrain Effects on an Upstate New York Tornado Event Utilizing a High-Resolution Model Simulation

LUKE J. LEBEL,[a] BRIAN H. TANG,[b] AND ROSS A. LAZEAR[b]

[a] *Department of Meteorology and Atmospheric Science, The Pennsylvania State University, University Park, Pennsylvania*
[b] *Department of Atmospheric and Environmental Sciences, University at Albany, State University of New York, Albany, New York*

(Manuscript received 14 February 2021, in final form 29 August 2021)

ABSTRACT: The complex terrain at the intersection of the Mohawk and Hudson valleys of New York has an impact on the development and evolution of severe convection in the region. Specifically, previous research has concluded that terrain-channeled flow in the Mohawk and Hudson valleys likely contributes to increased low-level wind shear and instability in the valleys during severe weather events such as the historic 31 May 1998 event that produced a strong (F3) tornado in Mechanicville, New York. The goal of this study is to further examine the impact of terrain channeling on severe convection by analyzing a high-resolution WRF Model simulation of the 31 May 1998 event. Results from the simulation suggest that terrain-channeled flow resulted in the localized formation of an enhanced low-level moisture gradient, resembling a dryline, at the intersection of the Mohawk and Hudson valleys. East of this boundary, the environment was characterized by stronger low-level wind shear and greater low-level moisture and instability, increasing tornadogenesis potential. A simulated supercell intensified after crossing the boundary, as the larger instability and streamwise vorticity of the low-level inflow was ingested into the supercell updraft. These results suggest that terrain can have a key role in producing mesoscale inhomogeneities that impact the evolution of severe convection. Recognition of these terrain-induced boundaries may help in anticipating where the risk of severe weather may be locally enhanced.

SIGNIFICANCE STATEMENT: On 31 May 1998, a widespread tornado outbreak occurred in the northeastern United States. One damaging tornado during the outbreak impacted the city of Mechanicville, New York. We used a high-resolution computer model simulation to examine how the topography of the region near Mechanicville affected the potential for tornado occurrence. We found that the topography contributed to the formation of an atmospheric boundary west of Mechanicville at the intersection of the Mohawk and Hudson valleys. The region to the east of the boundary was characterized as an environment particularly favorable for tornadoes. These results suggest that the identification of similar boundaries may be useful in increasing situational awareness of where the risk of severe weather may be locally enhanced.

KEYWORDS: Severe storms; Convective storms; Mesoscale processes

1. Introduction

The evolution of severe weather in the northeastern United States is complicated by the complex terrain of the region. Figure 1 shows a topographic map of a subset of the northeastern United States, including eastern New York and western New England, that will be the focus of this study. The important topographical features in this region include the north–south-oriented Hudson Valley and the west–east-oriented Mohawk Valley, which intersect near Schenectady (KSCH) and Albany (KALB), New York. The Adirondack Mountains lie north of the Mohawk Valley and west of the Hudson Valley, and the Catskill Mountains are located south of the Mohawk Valley.

The topographical features in the region modulate the occurrence of thunderstorms and severe weather. Wasula et al. (2002) determined that the spatial distributions of cloud-to-ground lightning and severe weather reports in the region are sensitive to the orientation of the synoptic-scale flow relative to these underlying terrain features. It was found that in cases with southwest flow, thunderstorms and severe weather reports are favored in the Mohawk Valley northward into the southern Adirondacks. In cases with northwest flow, thunderstorms and severe weather reports are most common in the southern Berkshire Mountains and Litchfield Hills of Connecticut. Katona et al. (2016) found that the mean High-Resolution Rapid Refresh (HRRR) model environment in the Hudson Valley is slightly more favorable for the potential of severe thunderstorms and tornadoes than the surrounding mountain regions, although the precise impact of terrain is again sensitive to the synoptic-scale wind direction.

One major mechanism through which terrain can influence the occurrence of severe weather is the terrain channeling of low-level flow. Terrain channeling occurs when terrain features, such as river valleys, act to change the local wind direction (Whiteman and Doran 1993). Terrain channeling has been observed during several tornado events in the northeastern United States. LaPenta et al. (2005) concluded that terrain-channeled flow in the Hudson Valley contributed to increased low-level wind shear and instability in the region where the 31 May 1998 Mechanicville, New York, tornado

Corresponding author: Luke J. LeBel, ljl5305@psu.edu

DOI: 10.1175/WAF-D-21-0018.1

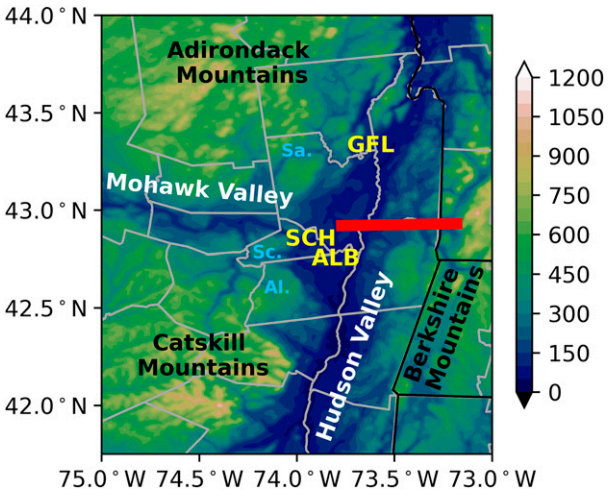

FIG. 1. Terrain height (m) in the region of interest. The locations of the Schenectady (SCH), Albany (ALB), and Glens Falls (GFL) airports are indicated. The red line is the track of the Mechanicville tornado. Saratoga County is denoted by Sa., Schenectady County is denoted by Sc., and Albany County is denoted by Al.

occurred. Similarly, Bosart et al. (2006) found that terrain-channeled southerly flow was present in the Hudson Valley on 29 May 1995 in the region where the Great Barrington, Massachusetts, tornado developed. They hypothesized that terrain channeling resulted in increased 0–1-km storm-relative helicity (SRH) and shear within the valley, increasing tornadogenesis potential. Bosart et al. (2006) further proposed that significant tornadoes are unlikely to occur in regions of complex terrain unless favorable local modifications to the low-level wind field are present. Tang et al. (2016) determined that channeled flow in the Hudson and Mohawk valleys contributed to enhanced moisture convergence, instability, and SRH in the region where the 22 May 2014 Duanesburg, New York, tornado developed. Outside the northeastern United States, flow channeling has also been found to influence the potential for severe weather in other prominent river valleys, such as the Upper Rhine Valley in Germany (Hannesen et al. 1998).

Previous research on severe weather events in the northeastern United States has been limited by the sparse observational network in the region. Studies such as LaPenta et al. (2005) and Bosart et al. (2006) relied on observational sources available at that time, including radar data, satellite data, upper-air soundings, and surface observations to assess hypotheses about the role of terrain in tornado cases. Surface observations were particularly important in establishing the presence of channeled flow in the Hudson Valley for these cases, but the specific effects of the channeled flow on the convective evolution were largely speculative. Until more recently, studies did not have access to high-resolution model output that could provide additional analysis of the role of terrain in modulating the environment and impacting the convective evolution.

Previous model-based studies of the effects of terrain on severe convection have used both idealized and real-data simulations to explore this topic. For example, Markowski and Dotzek (2011) simulated convection as it passed over idealized plateaus, valleys, and mountains. Such idealized studies are useful for understanding the fundamental mechanisms through which terrain can modify the environments for severe weather and impact the evolution of convection. Other studies have simulated convection in real terrain, allowing for a better understanding of how actual terrain features can impact the environment for, and evolution of, severe convection. For example, Geerts et al. (2009) utilized the Weather Research and Forecasting (WRF) Model to analyze the role of terrain on an unusual tornadic mesocyclone that occurred in the high terrain of southeastern Wyoming. Homar et al. (2003) utilized the fifth-generation Pennsylvania State University–National Center for Atmospheric Research Mesoscale Model (MM5) to analyze a tornado event over northeastern Spain. Kovacs and Kirshbaum (2016) used a quasi-idealized modeling framework to examine how the terrain of southern Quebec influences the climatology of deep convection in the region. A high-resolution simulation of the 31 May 1998 Mechanicville, New York, tornado event will be presented herein to examine the impact of terrain on the mesoscale environment and convection, and to complement the observational analysis conducted by LaPenta et al. (2005).

In addition to the impact of terrain through flow channeling, other mechanisms of mesoscale variability have also been found to increase the potential for tornadoes. Mesoscale boundaries have been associated with past tornado events (Maddox et al. 1980). Markowski et al. (1998) found that nearly 70% of significant tornadoes in the Verification of the Origins of Rotation in Tornadoes Experiment (VORTEX) field campaign were associated with boundaries, and therefore concluded that boundaries may play a role in tornadogenesis in certain cases. Boundaries have been found to enhance significant tornado potential by increasing the SRH (Rasmussen et al. 2000), and by deepening the boundary layer moisture and augmenting low-level horizontal vorticity through the baroclinic generation of vorticity (Markowski and Richardson 2009). Additionally, Atkins et al. (1999) found in an idealized framework that the "cool" side of a boundary acted as a source of streamwise vorticity for the updraft. In their analysis of the Duanesburg tornado, Tang et al. (2016) documented that a north–south oriented boundary developed in the Hudson and Mohawk valleys on 22 May 2014. This boundary separated a maritime air mass to the east from a more unstable air mass to the west and was maintained by differential surface heating. The Duanesburg tornado developed as a supercell crossed this boundary into an environment characterized by strong 0–1-km wind shear, low lifting condensation levels (LCLs), and large values of streamwise vorticity.

Streamwise vorticity, a measure of the potential for inflow parcels to produce net cyclonic updraft rotation (Davies-Jones 1984), has been identified as a useful variable in the analysis of supercell thunderstorms. The tilting and stretching of streamwise vorticity is an important source of vertical vorticity within supercell updrafts (e.g., Rotunno and Klemp 1985; Markowski and Richardson 2009). Climatologies of observed (Rasmussen and Blanchard 1998) and model (Markowski et al. 2003) proximity soundings have demonstrated that low-level wind shear and streamwise vorticity are important for significant tornado formation. Markowski et al. (2003) found that the streamwise vorticity in the lowest 1 km above ground level

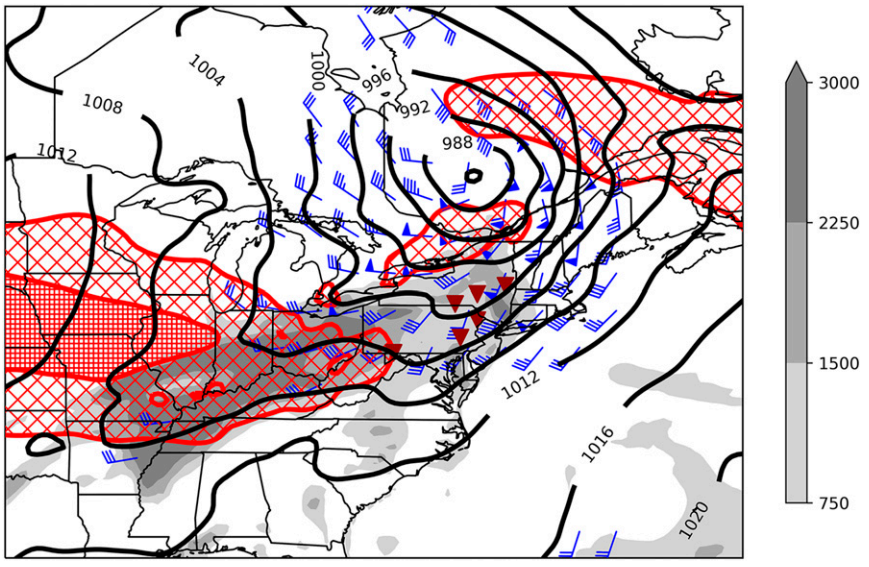

FIG. 2. Synoptic analysis at 2000 UTC 31 May 1998, showing 200-hPa wind speed (coarse red hatching for wind speeds between 40 and 60 m s^{-1}; fine red hatching for wind speeds greater than 60 m s^{-1}), 850-hPa winds (blue barbs; half barb = 2.5 m s^{-1}, full barb = 5 m s^{-1}, pennant = 25 m s^{-1}), mean sea level pressure (black contours every 4 hPa, smoothed using a 12-point Gaussian filter), and most unstable convective available potential energy (gray shading; J kg^{-1}). The dark red triangles indicate the locations of the six F3 tornadoes. Fields are from the ERA5 reanalysis (European Centre for Medium-Range Weather Forecasts 2017).

(AGL) is significantly larger in the environments of ''significantly tornadic'' (EF/F2–EF/F5) supercells than of nontornadic supercells. Parker (2014) developed composite proximity soundings for the tornadic and nontornadic supercells observed by the second Verification of the Origins of Rotation in Tornadoes Experiment (VORTEX2) and found that the tornadic wind profile was characterized by more low-level streamwise vorticity than the nontornadic profile. In simulations using these soundings (Coffer and Parker 2017; Coffer et al. 2017; Coffer and Parker 2018), the orientation of the near-surface horizontal vorticity played a dominant role in the organization of the low-level mesocyclone. Enhanced low-level streamwise vorticity in the tornadic wind profile resulted in simulated supercells with robust and steady low-level mesocyclones that favored tornadogenesis. Therefore, the tilting of streamwise vorticity represents an important stage in the tornadogenesis process (Davies-Jones 2015).

Streamwise vorticity can be diagnosed operationally utilizing SRH. The calculation of SRH features contributions from storm-relative flow and streamwise vorticity. Peters et al. (2020) found that the primary role of streamwise vorticity is to increase the low-level updraft and rotation, while the storm-relative winds play an important role in determining important updraft properties such as updraft width. Low-level SRH—especially in the lowest 500 m AGL—is effective at discriminating between significantly tornadic supercells and nontornadic supercells (Esterheld and Giuliano 2008; Coffer et al. 2019). Because streamwise vorticity is strongly connected with tornadogenesis, it is important to understand how mechanisms of mesoscale variability, including the impact of terrain through flow channeling and mesoscale boundaries, impact the distribution and magnitude of low-level streamwise vorticity.

This study will focus on the mesoscale characteristics, and particularly the terrain-induced inhomogeneities in the convective environment, of the 31 May 1998 Mechanicville, New York, event. Beforehand, we briefly describe the synoptic setup for the widespread severe weather outbreak here. The outbreak occurred in the warm sector of a deepening surface cyclone. At 2000 UTC 31 May (just prior to the occurrence of the Mechanicville tornado from 2022 to 2055 UTC), this surface cyclone was located over southwestern Quebec, with a minimum central pressure below 984 hPa (Fig. 2). This cyclone was positioned in a region of strong forcing for ascent, as coupled jet streaks were present over southern Quebec at 200 hPa. To the south of the surface cyclone, a strong 850-hPa jet (>25 m s^{-1}) was located over the northeastern United States. This jet advected a moist, unstable air mass into New York. A large region of most unstable convective available potential energy > 750 J kg^{-1} was present, extending from New York south and west into the Ohio Valley. Additionally, the strong low-level jet coincided with significant low-level wind shear across the warm sector. The reader is referred to LaPenta et al. (2005) for a more thorough discussion of the synoptic characteristics of this event.

Consistent with the very favorable environment for severe weather in place, the Storm Prediction Center issued a ''High Risk'' for severe thunderstorms, including tornadoes, for much of New York and Pennsylvania. This was the first ever High Risk issued for New York and Pennsylvania. The resulting severe convection produced 39 tornadoes (1200 UTC 31 May–1200 UTC 1 June) across a broad region extending from the Ohio Valley through the northeastern United States, including six F3 tornadoes.

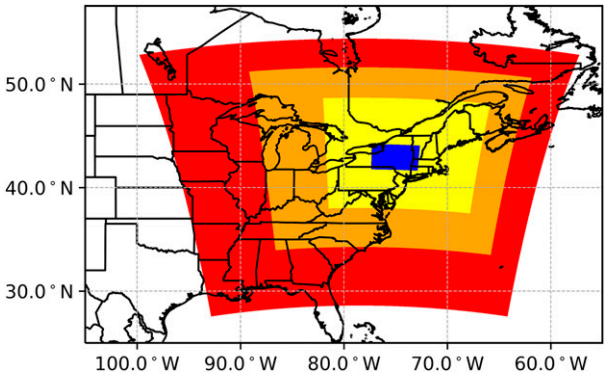

FIG. 3. WRF simulation domains (27-km domain is red, 9-km domain is orange, 3-km domain is yellow, and 1-km domain is blue).

The Mechanicville tornado was the farthest northeast of these six F3 tornadoes (Fig. 2). The evolution of convection leading up to the Mechanicville tornado was complex, involving the merger between a supercell with an advancing squall line near the time of tornadogenesis (see LaPenta et al. 2005; section 5). In this paper, we use a high-resolution WRF Model simulation to examine the possible impact of terrain-induced inhomogeneities on the convection associated with the Mechanicville tornado.

The remainder of the paper is structured as follows. A description of the model configuration and verification of the model performance is provided in section 2. Section 3 focuses on the mesoscale characteristics of the event, including the impact of terrain, and section 4 discusses the impact of the mesoscale environment on storm-scale processes. A discussion of the event characteristics is presented in section 5, and conclusions are provided in section 6.

2. Methodology

The Advanced Research version of WRF (WRF-ARW) version 3.9.1.1 (Skamarock et al. 2008) was used to simulate the 31 May 1998 severe weather event in eastern New York. The simulation employed four two-way nested domains (Fig. 3), and the horizontal grid spacing of the domains varied from 27 km in the outermost domain to 1 km for the innermost domain. The innermost domain covered parts of New York and western New England and was the primary domain of interest to examine the impact of terrain. Table 1 gives the model configuration and parameterization schemes used in this simulation, which are largely similar to the operational HRRR model (Benjamin et al. 2016).

The model was initialized at 1500 UTC 31 May, and the North American Regional Reanalysis (NARR) dataset (Mesinger et al. 2006) provided the initial and boundary conditions for the cold-start simulation. The initialization time is around 5 h before the occurrence of the tornado. A variety of different combinations of initialization times (0000–1500 UTC 31 May) and initial and boundary condition data sources (e.g., Climate Forecast System Reanalysis) were tested, and it was determined that this configuration resulted in a simulation that closely matched available surface observations and the 1800 UTC 31 May upper-air sounding from Albany, New York. A comparison of the simulation against these observations is presented later in this section.

TABLE 1. WRF Model parameters and parameterizations used in this study.

Model parameter	Option used
Horizontal grid spacing	27/9/3/1 km
Vertical levels	36, 100-hPa model top
Cumulus parameterization scheme	Grell–Freitas ensemble scheme (27-km domain only; Grell and Freitas 2014)
Microphysics scheme	Aerosol-aware Thompson scheme (Thompson and Eidhammer 2014)
Planetary boundary layer scheme	MYNN 2.5-level TKE scheme (Nakanishi and Niino 2006), with the MYNN surface layer
Land surface scheme	Unified Noah land surface model (Chen and Dudhia 2001)
Radiation	RRTMG scheme (both shortwave and longwave; Iacono et al. 2008)

The simulation did not produce a supercell that closely matched the observed path of the Mechanicville supercell. This deficiency is not surprising, as it is unreasonable to expect a cold-start simulation to reproduce the observed storm evolution. The simulation of convection initiation is very sensitive to small perturbations in low-level temperature, moisture, and wind (e.g., Martin and Xue 2006; Hill et al. 2016), and to boundary layer convection (e.g., Xue and Martin 2006). Additionally, the Mechanicville supercell did not initiate along a synoptic frontal boundary, and convection initiation may have been sensitive to the evolution of upstream convection (LaPenta et al. 2005). One goal of this study is to examine the storm-scale interactions between a supercell and the complex terrain of upstate New York in the vicinity of Mechanicville, and so it is critical to address this deficiency. Therefore, an idealized convection initiation technique was used. A warm bubble, 30 km in diameter and 3.5 km deep, was inserted into the model at 1700 UTC (2 h into the simulation) in the lower troposphere to trigger the development of a thunderstorm that followed closely to the observed track of the Mechanicville supercell. The location of the warm bubble was determined by extrapolating the path of the true Mechanicville supercell backward to 1700 UTC. The maximum potential temperature perturbation in the center of warm bubble was 8 K, and the perturbation decreased linearly with radius. Compared to previous idealized studies that have utilized a warm bubble to trigger convection (e.g., Nowotarski et al. 2011; French and Parker 2014), the magnitude of the maximum potential temperature perturbation used here is unusually large. Sensitivity testing revealed that 8 K was the magnitude necessary to produce a sustained supercell in this simulation for the methodology used (not shown). The insertion of the warm bubble, and any short-term unbalanced response to the bubble, did not have any discernible effect on the environment away from the bubble itself. The resulting triggered supercell closely followed the observed track of the true Mechanicville supercell, as will be discussed in the following section.

Model evaluation

We perform an evaluation of the simulation against available observations to assess the accuracy of the simulated

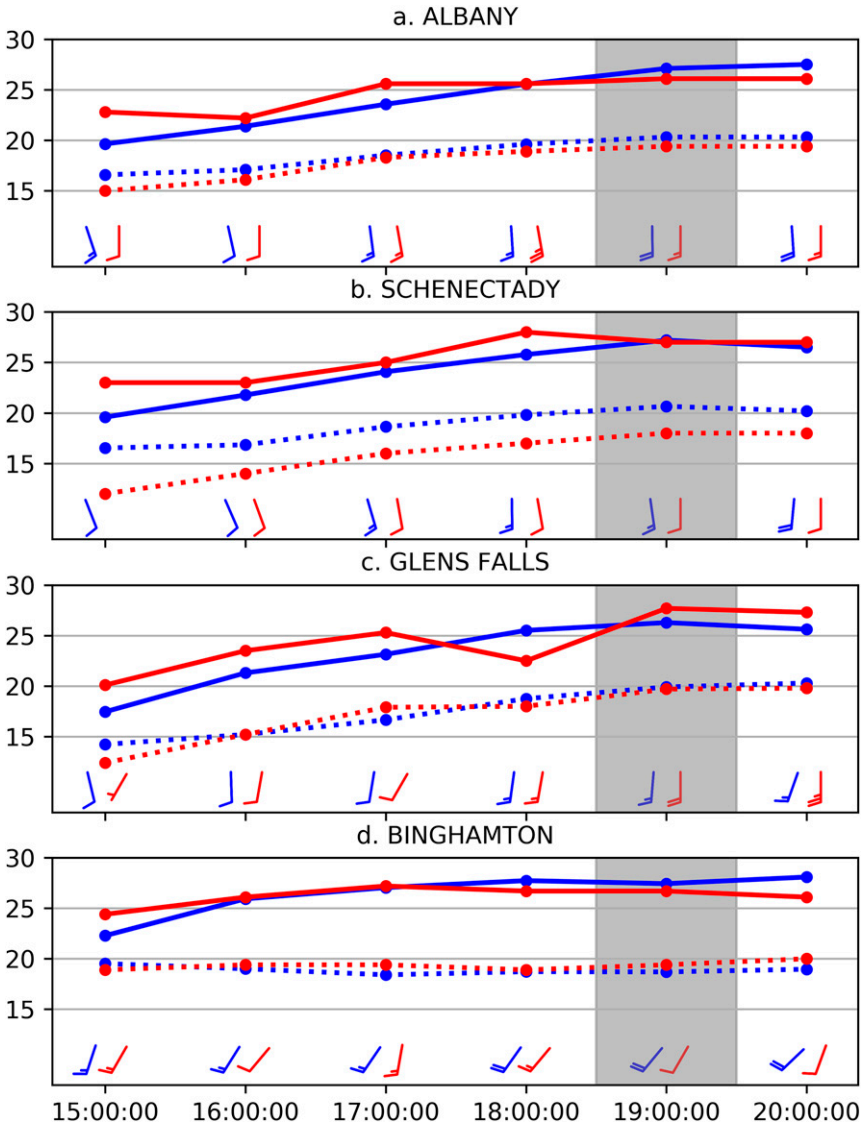

FIG. 4. A comparison between simulated (blue) and observed (red) temperatures (°C; solid lines), dewpoint temperatures (°C; dashed lines), and winds (barbs; m s^{-1} as in Fig. 2) for (a) KALB, (b) KSCH, (c) KGFL, and (d) KBGM. The shaded area highlights the critical, prestorm period.

environment in order to support the use of this simulation to analyze mesoscale features that were unresolved by available observations. Figure 4 shows a comparison between Hudson Valley surface METAR observations from KSCH, KALB, and Glens Falls, New York (KGFL), and model output at the closest grid point. The observations from Binghamton, New York (KBGM; located 189 km to the west-southwest of KALB), will be discussed as well, because these observations best reflect the nonchanneled flow over higher terrain in central New York. In general, the model simulation compared well to these surface observations. In particular, the model closely matched observations in the immediate preconvective environment at 1900 UTC (shaded interval on Fig. 4). At 1900 UTC, the KALB, KSCH, and KGFL temperature and dewpoint errors were all small (generally within 1°C). At KALB, the simulation was too warm by 1.0°C and too moist by 0.9°C (Fig. 4a). The largest dewpoint errors were at KSCH, where the simulated dewpoint temperature was consistently 2°–3°C too high (Fig. 4b) but might be due to systematic instrument error. A comparison between the KSCH and KALB dewpoint observations on the preceding days indicated that the KSCH dewpoints were consistently lower than at KALB, despite the stations only being 16 km apart (not shown). The simulated winds at these locations were also similar to observations, indicating that the simulation reproduced the channeled, southerly flow within the Hudson Valley. Outside of the valley at KBGM (Fig. 4d), the model simulation similarly performed well. At 1900 UTC, the temperature and dewpoint errors were both less than 1°C at KBGM. The simulated wind direction was also similar to the observed wind direction, although there were differences in

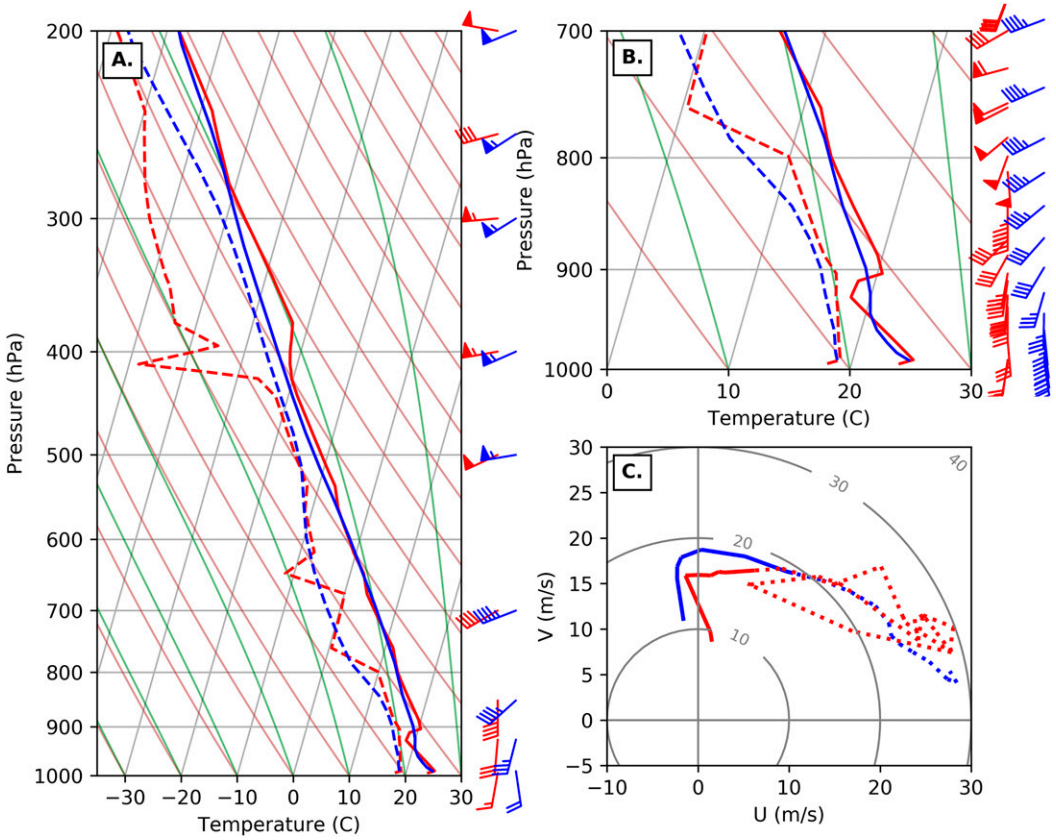

FIG. 5. A comparison between the 1800 UTC Albany, New York, sounding (red) and a simulated profile at the same location (blue). (a) The temperature (solid; °C), dewpoint (dashed; °C), and mandatory-level winds (barbs; m s^{-1} as in Fig. 2) for the profiles. (b) The temperature, dewpoint, and winds below 700 hPa. (c) Hodographs for the simulated (blue) and observed winds (red), neglecting questionable observations between 850 and 799 hPa. The solid lines are winds in the 0–1-km layer, and the dashed lines are winds in the 1–6-km layer.

wind speed. Overall, the low errors at 1900 UTC suggest that the model represented the near-surface conditions of the critical period in the prestorm environment well.

Additionally, the model simulation is verified against the observed 1800 UTC 31 May upper-air sounding from Albany, New York. Figure 5 shows a comparison between the observed 1800 UTC sounding and a simulated profile at Albany, New York. The comparison indicates that the simulation reasonably depicted the overall vertical structure of the temperature, dewpoint, and winds (Fig. 5a). Below 700 hPa, the simulation adequately captured the low-level temperature and wind profiles (Fig. 5b). There are, however, some notable differences between the profiles, which primarily result from the smoothed appearance of the simulated sounding vertical structure compared to the observed sounding. The simulation underpredicted both the magnitude of the stable layer just below 900 hPa and the depth of the boundary layer. Nonetheless, the model exhibits a smoothed representation of a shallow boundary layer beneath a stable layer. The simulated wind profile closely matched the observed wind profile below 900 hPa, although the winds were more southwesterly near 925 hPa in the simulation than in observations. The southerly flow through the depth of the boundary layer in both the simulated and observed sounding is the manifestation of terrain channeling (LaPenta et al. 2005).

The observed wind profile contained questionable winds in the 850–799-hPa layer (Fig. 5b; see LaPenta et al. 2005). To confirm these were likely erroneous, the KENX (Albany) radar VAD wind profiles around 1800 UTC were examined, and they did not display the unexpected "veer–back–veer" profile contained in the observed sounding. A comparison between the observed and simulated hodographs, with the questionable observed winds between 850 and 799 hPa omitted, is presented in Fig. 5c. The hodographs both contain strong curvature in the lowest 1 km. Overall, this comparison suggests that the simulation did an adequate job representing the pre-storm environment, including both the vertical profile at Albany and the surface conditions in the area of interest. Therefore, we have confidence that results from the simulation can represent and be used to study poorly observed mesoscale features that may have played a role in the convective evolution.

The supercell initiated by the warm bubble progressed through southern Saratoga County (and the Mechanicville region) between 2000 and 2030 UTC. The growth and location

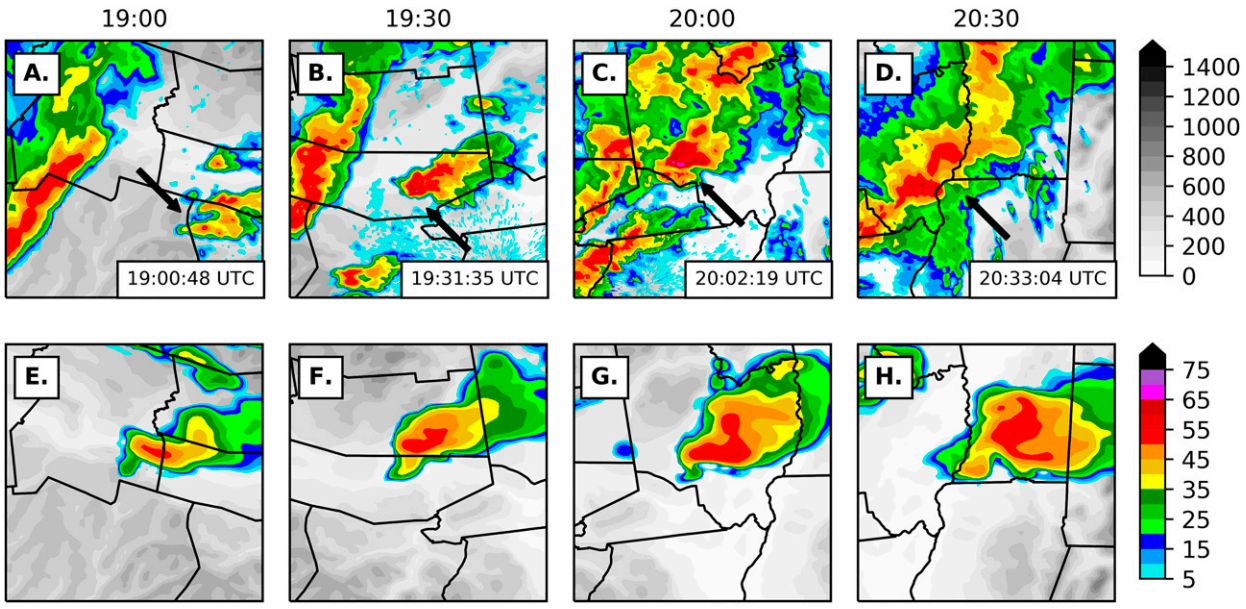

FIG. 6. (top) Observed and (bottom) simulated radar reflectivity (dBZ) at (a),(e) 1900; (b),(f) 1930; (c),(g) 2000; and (d),(h) 2030 UTC. The images are centered on the location of mesocyclone in the simulated supercell. The gray shading indicates terrain height (m). The black arrows indicate the location of the observed supercell.

of the simulated supercell are similar to the evolution of the observed Mechanicville supercell (Fig. 6), although there are notable differences in the coverage and complexity of convective storms. The primary difference is that the observed supercell merged with an advancing squall line near the time of tornadogenesis. The simulation therefore does not capture the storm-scale interactions associated with the complex convective evolution on 31 May 1998, and instead isolates on a primary goal of this study which is the effects of terrain on the mesoscale environment and simulated supercell. A discussion of the possible role of the merger will be presented in section 5. A second difference between the simulated and observed supercell is that the simulated supercell tracked slightly more quickly to the east. Overall, this difference is small, and both the simulated and observed supercells were in a similar location at 1930–2000 UTC, when the supercell entered the Hudson Valley.

3. Mesoscale characteristics

The modeled mesoscale environment in upstate New York evolved rapidly on 31 May 1998 due to temperature and moisture advection associated with a synoptic-scale warm front in the region. Distinct from this warm front, we will show that a sharp localized mesobeta-scale boundary, characterized at the surface by a distinct wind shift and moisture gradient, developed at the intersection of the Hudson and Mohawk valleys in the WRF simulation. This boundary was not possible to detect in real time, due to the sparse observational network in the region in 1998. The remainder of this section will focus on the development and characteristics of this boundary.

a. Boundary development

The boundary developed rapidly in the proximity of a broad synoptic-scale warm frontal zone that progressed through the region. At 1600 UTC, the presence of this warm front is apparent in the model simulation as a gradient in surface potential temperature θ across the region (Fig. 7a). Surface equivalent potential temperatures $\theta_e > 338$ K were present over the elevated terrain of the Catskill Mountains, as the warm-sector air was advected into the region by strengthening southwesterly flow. However, the θ_e within the Hudson and Mohawk valleys remained comparatively lower. Additionally, a clear signal of terrain channeling was apparent within both valleys. East-southeasterly winds in the Mohawk Valley and south-southeasterly flow in the Hudson Valley existed on the cool side of the warm front (Fig. 7a). Dewpoints within the Hudson Valley were relatively low, between 17° and 18°C near KALB (Fig. 7b).

By 1700 UTC, the mesoscale boundary development at low elevations within the intersection of the Mohawk and Hudson valleys had commenced. The channeled flow identified at 1600 UTC remained, and at 1700 UTC the wind shift associated with flow channeling extended northward into the lower elevations of the Mohawk Valley (Fig. 8a). Moisture convergence (not shown) and near-surface frontogenesis were occurring along the incipient boundary (Fig. 8b), supporting the increase of moisture along and east of the boundary. The southern portion of the frontogenesis axis closely follows the 500-m elevation contour, suggesting an association between terrain features and the initial position of the boundary. Additionally, at 1700 UTC, higher moisture air began to surge into the southern Hudson Valley. In the simulation, dewpoints > 20°C moved rapidly into southern portions of the Hudson Valley (Fig. 8b) and were advected northward in strong southerly terrain-channeled flow (Fig. 8a). Observations support the occurrence of this moisture surge. Surface observations from Poughkeepsie, New York, recorded an increase in dewpoint to above 20°C (south of the map domain, not shown).

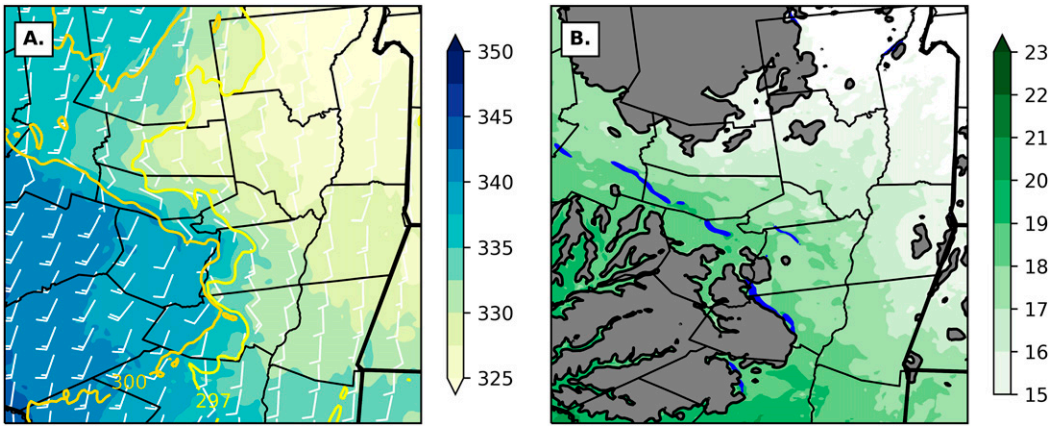

FIG. 7. Mesoscale analysis for 1600 UTC 31 May: (a) θ_e at the lowest model level (K; shaded), θ at the lowest model level (K; 297 K in yellow, 300 K in gold, and 303 K in orange), and 10-m winds (barbs; m s^{-1} as in Fig. 2); (b) 2-m dewpoint (°C), near-surface two-dimensional θ frontogenesis > 3 K km^{-1} h^{-1} (blue) and terrain height > 500 m (gray).

Due to this moisture surge, θ_e values began to increase within the Hudson Valley, although θ_e values remained higher farther west in the higher terrain where potential temperatures were warmer.

At 1800 UTC, the surge of moisture up the Hudson Valley continued, with dewpoints > 20°C reaching as far north as Saratoga County (Fig. 9b). This surge of moisture was driven by strong southerly and south-southeasterly terrain-channeled surface winds within the Hudson Valley (Fig. 9a). As moisture increased within the Hudson Valley, a north–south-oriented moisture gradient was becoming established at the intersection of the Hudson and Mohawk valleys, coincident with an axis of frontogenesis (Fig. 9b). These trends continued through 1900 UTC, which represented the near-storm environment. At 1900 UTC, the boundary was more defined, as seen by the increased moisture and θ gradient at the intersection of the Mohawk and Hudson valleys (Fig. 10). Within the Hudson Valley, dewpoints were >20°–21°C in strong southerly terrain-channeled flow. Farther west in the Mohawk Valley, dewpoints were around 18°–19°C in southwesterly flow. These values were lower than the previous hour, suggesting that mixing of drier air from aloft, horizontal advection of drier air, and/or downslope flow to the west of the boundary was contributing to the increased gradient of moisture across the boundary. Additionally, in response to the increase in moisture along and east of the boundary, a local maximum in θ_e began to develop along and east of the surface wind shift by 1900 UTC. Values of $\theta_e > 345$ K were present in northwestern Albany County and Schenectady County (Fig. 10a).

To better understand the development and intensification of this boundary, back trajectories were calculated surrounding the boundary location utilizing the Lagrangian Analysis Tool (LAGRANTO; Sprenger and Wernli 2015). Trajectories were calculated from 1-min WRF output with an integration time step of 6 s. The 30-min back trajectories from 1930 UTC were calculated for parcels within a box surrounding the boundary at and south of the intersection of the Hudson and Mohawk valleys. The trajectories were all initialized at 500 m above mean sea level (MSL) at 1930 UTC to capture the near-surface flow. The back trajectories clearly indicate the different source regions of air parcels to the immediate west and east of the boundary (Fig. 11). To the east of the boundary,

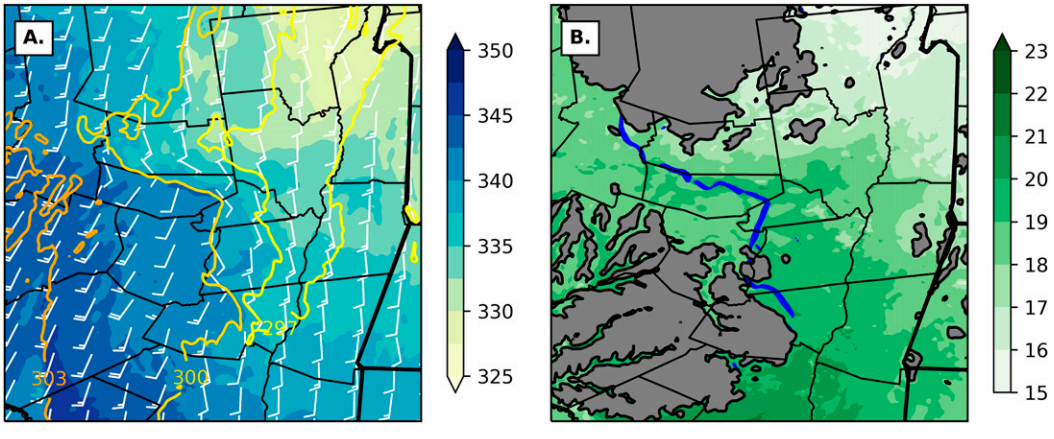

FIG. 8. As in Fig. 7, but for 1700 UTC.

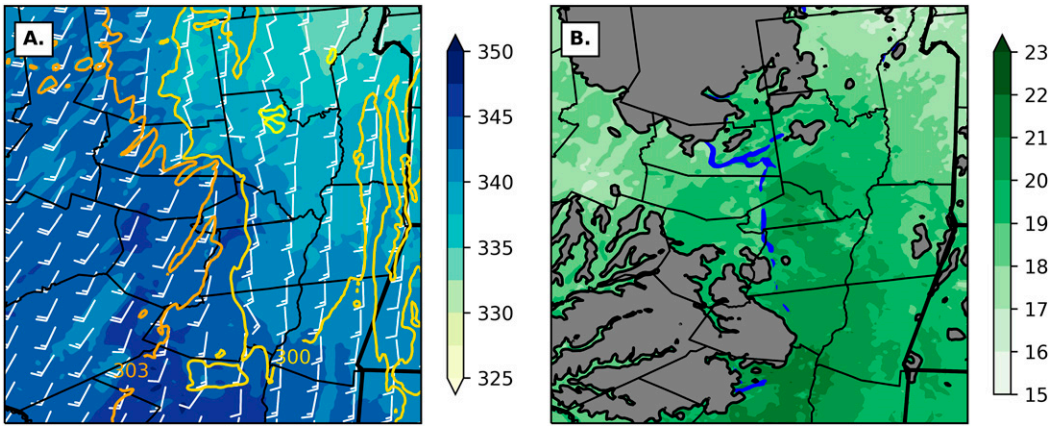

FIG. 9. As in Fig. 7, but for 1800 UTC

parcels characterized by relatively low θ and high water vapor mixing ratios tracked toward the boundary from the south and south-southeast, especially in the low elevations near the intersection of the Mohawk and Hudson valleys (Fig. 11a). To the west of the boundary, air parcels with higher θ and lower mixing ratios tracked toward the boundary from the southwest. These trajectories imply the presence of downsloping to the west of the boundary, as many of the trajectories originated over terrain elevations exceeding 500 m. In fact, several of the trajectories that were located west of the boundary and within the Mohawk Valley at 1930 UTC descended over 500 m from their 1900 UTC location (Fig. 11b). These trajectories therefore reflect the extension of the potentially warm and relatively dry boundary layer present over the Catskill Mountains downward to the Mohawk Valley floor. The juxtaposition of this relatively dry boundary layer with the channeled moist flow within the Hudson Valley established the moisture gradient at the valley intersection and facilitated the development of the boundary. Confluence in the lee of the Catskills, apparent in Fig. 11, supported the tightening of the θ and moisture gradients farther north near the intersection of the Mohawk and Hudson valleys.

b. *Boundary characteristics*

We now analyze the vertical structure of the boundary. Figure 12 presents vertical cross sections across the boundary at two different locations denoted in Fig. 10b at 1900 UTC, when the boundary was well developed and not yet disturbed by convection. As will be discussed below, the supercell that was triggered by the warm bubble interacted with the boundary between 1930 and 2000 UTC. Therefore, the characteristics of the boundary at 1900 UTC capture the state of the boundary preceding the interaction of the supercell with the boundary.

The cross sections in Fig. 12 highlight several important aspects of the structure of the boundary. First, the boundary is characterized by a horizontal gradient in potential temperature in the lowest 1 km. This potential temperature gradient is strongest in the northern cross section, to the west of Mechanicville (Fig. 12a), although a more diffuse and weaker gradient is still present in the southern cross section. The

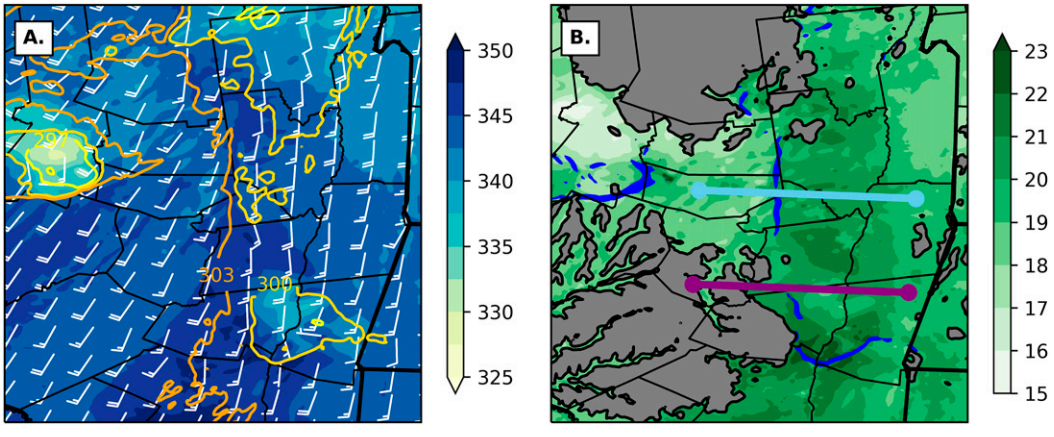

FIG. 10. As in Fig. 7, but for 1900 UTC. The light blue and purple lines indicate the locations of the northern and southern cross sections, respectively, in Fig. 12.

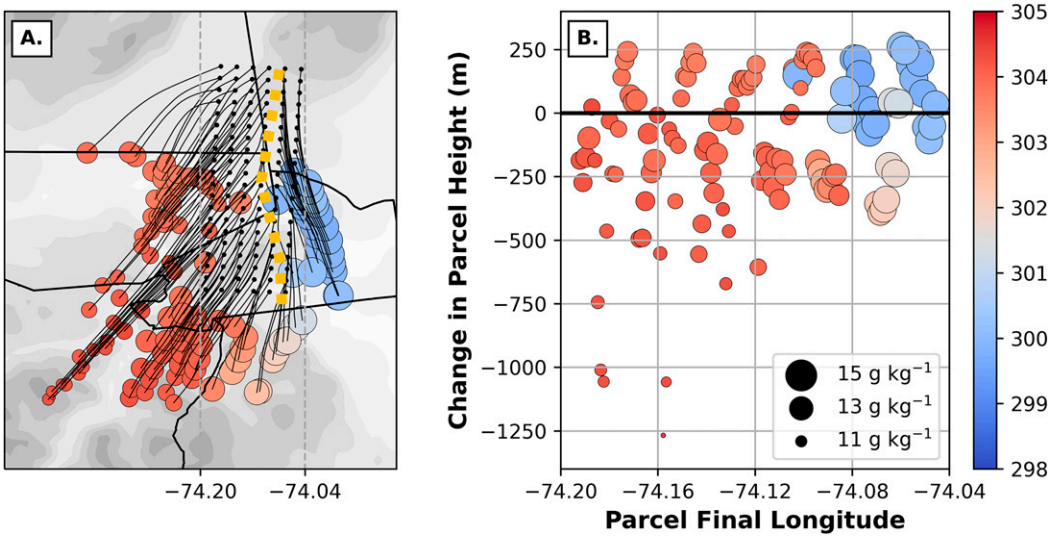

FIG. 11. (a) 30-min back trajectories from 1930 UTC around the boundary. The shaded dots indicate the location of the parcel at 1900 UTC, the shading indicates the θ of the parcel at 1900 UTC, and the size of the dots indicate water vapor mixing ratio (g kg^{-1}). The black dots on the trajectories indicate the location of the parcel at 1930 UTC. The orange, dashed line indicates the approximate location from the boundary. The gray shading indicates terrain height (following Fig. 6). (b) The final longitude of the parcel plotted against the change in parcel height from 1900 to 1930 UTC. Negative values indicate net descent. The shading and size of the dots follow the same convention as in (a).

stronger potential temperature gradient in the northern cross section is consistent with the area of stronger frontogenesis in Fig. 10b. Additionally, the back trajectories presented in Fig. 11 suggest that confluence in the lee of the higher terrain features in the Catskill Mountains supported the strengthening of the gradient in the northern portion of the boundary. Second, the boundary is characterized by a distinct wind shift in the lowest 1 km. This wind shift is only evident along the northern end of the boundary, where strong south-southeasterly, terrain-channeled flow was present on the cool and moist (Fig. 10b) side of the boundary below 500 m (Fig. 12a). Third, there is a clear gradient in stability across the boundary, with deep mixing to around 2 km MSL to the west of the boundary, and a stable layer at 0.5–1 km MSL east of the boundary

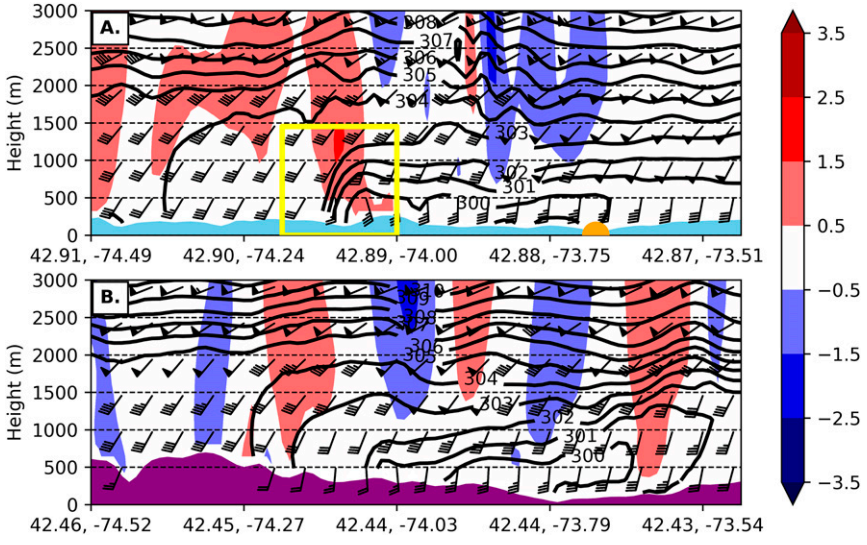

FIG. 12. (a),(b) Cross sections at 1900 UTC 31 May of vertical motion (m s^{-1}; fill), horizontal winds (barbs; m s^{-1} as in Fig. 2), and potential temperature (contoured; K). Locations of cross sections are denoted in Fig. 10. The colors of the terrain height correspond to the colors of the location indicators in Fig. 10. The orange semicircle in (a) indicates the longitude of Mechanicville, and the yellow box in (a) encloses the region of the boundary.

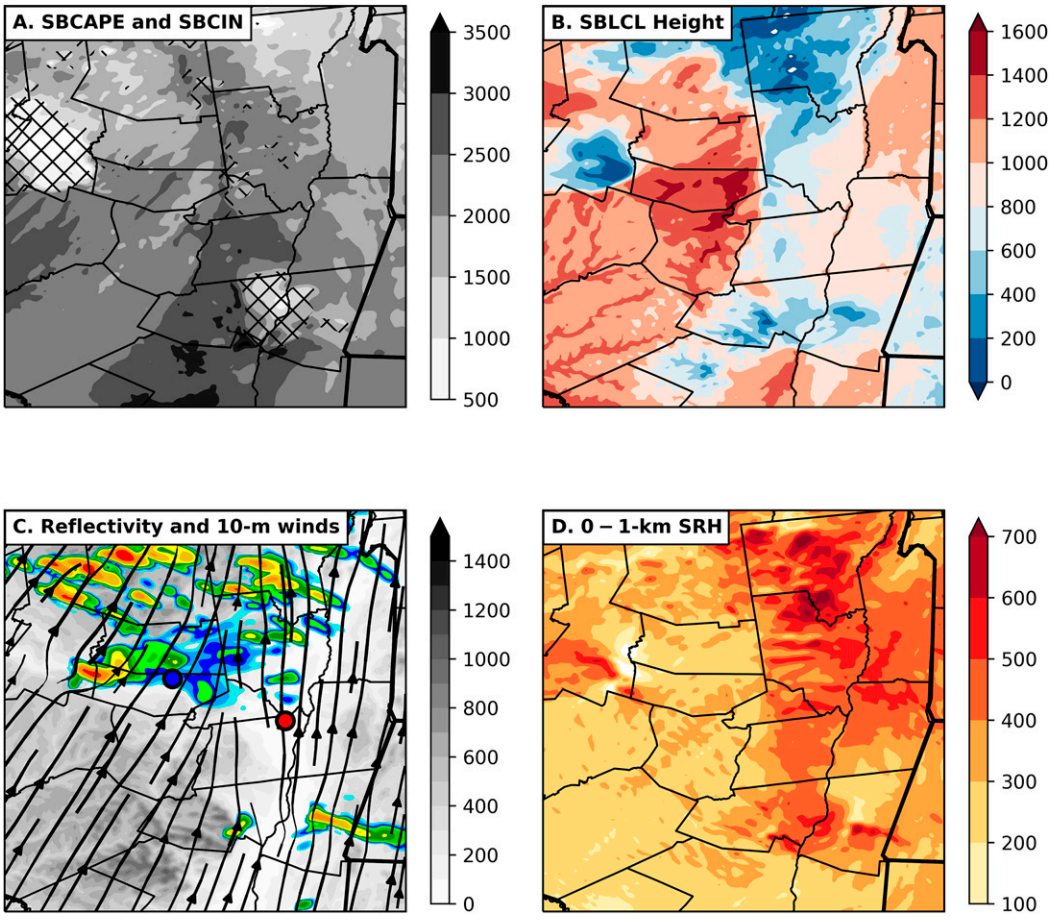

FIG. 13. Severe weather parameters at 1900 UTC. (a) SBCAPE (J kg^{-1}) and SBCIN < -25 J kg^{-1} (hatches); (b) the SBLCL height AGL (m); (c) terrain height (m; color bar), 1 km AGL simulated reflectivity (dB*Z*; color following Fig. 6), and 10-m streamlines; and (d) 0–1 km AGL SRH (m^2 s^{-2}). The blue and red dots in (c) correspond to the locations of the hodographs in Fig. 14.

(Figs. 12a,b). This stable layer was sampled by the observed 1800 UTC Albany sounding (Fig. 5b). Finally, there is ascent in the vicinity of the boundary, especially along and to the immediate west of the boundary in the northern cross section.

Consistent with the structure described above, there was a large difference in severe weather parameter magnitudes across the boundary. While these parameters were supportive of severe convection and tornadoes in the entire region, the region immediately east of the boundary (near Mechanicville) was characterized by an especially favorable environment for severe weather and tornadogenesis (Fig. 13). At 1900 UTC, in the immediate prestorm environment, surface convective available potential energy (SBCAPE) was maximized along and east of the boundary (Fig. 13a), where SBCAPE exceeded 2500 J kg^{-1}. This axis of high SBCAPE corresponded with the axis of high surface θ_e air (Fig. 10a). Additionally, the increase in moisture to the east of the boundary contributed to a lower surface based LCL (SBLCL). The SBLCL heights to the east of the boundary were near 600 m AGL in a narrow axis, while the SBLCL heights to the west of the boundary were between 1000 and 1400 m AGL (Fig. 13b). Lower LCL heights have been found to be a favorable factor for significant tornadoes (Thompson et al. 2003). Kinematically, the south-southeasterly winds present within the Hudson Valley east of the boundary (Fig. 13c) contributed to increased low-level wind shear to the east of the boundary. The 0–1-km SRH west of the boundary was commonly between 200 and 300 m^2 s^{-2}, while the 0–1-km SRH east of the boundary was >400 m^2 s^{-2} (Fig. 13d). This difference in 0–1-km SRH can be seen graphically from the hodographs west and east of the boundary (Fig. 14). There is much more clockwise hodograph curvature in the lowest 1 km AGL to the east of the boundary than farther west in the Mohawk Valley or near KBGM (cf. with LaPenta et al. 2005, their Fig. 17). The values of 0–1-km SRH within the Hudson Valley are near the 90th percentile of model proximity soundings in advance of significantly tornadic supercells analyzed in Thompson et al. (2007), highlighting the extreme nature of the low-level wind shear within the Hudson Valley. These values of 0–1-km SRH are near the highest values observed during May and June at Albany, New York, according to the Storm Prediction Center sounding climatology (Rogers et al. 2021). Additionally, the

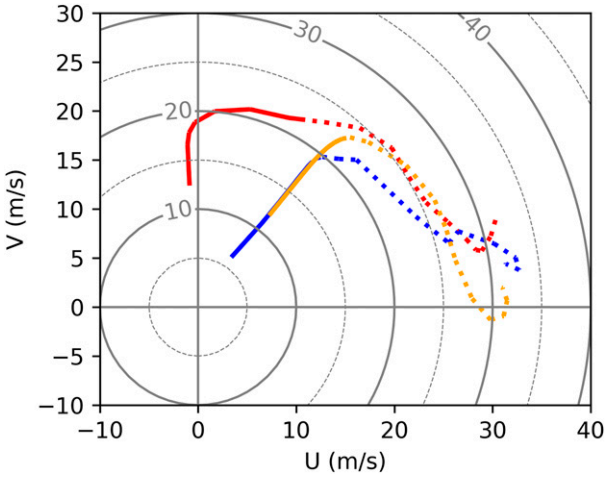

FIG. 14. Hodographs corresponding to a location west of the boundary (blue), east of the boundary (red), and at the closest model grid point to KBGM (orange). The solid portions of the line are the 0–1 km AGL layer, and the dashed portions of the line are the 1–6 km AGL layer.

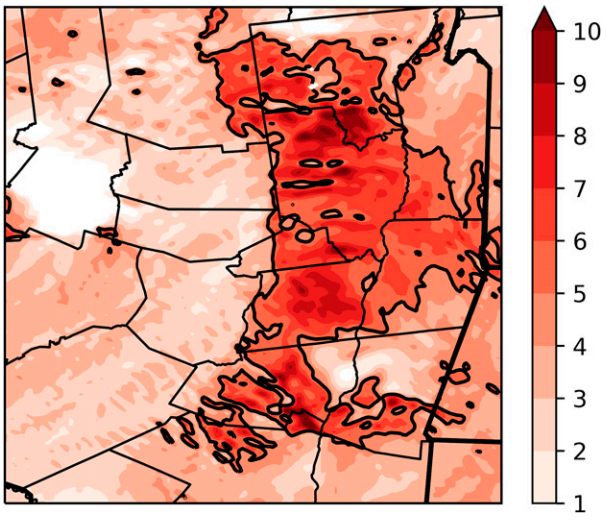

FIG. 15. The significant tornado parameter (STP) at 1900 UTC. The black contour encloses the region of STP > 5.

significant tornado parameter (STP) was calculated using the equation in Thompson et al. (2012) modified to use surface lifted parcels and fixed-layer shear. Most significant tornadoes occur with STP > 1. At 1900 UTC, values of STP to the west of the boundary were generally between 2 and 4, indicating an environment supportive of significant tornadoes. East of the boundary, STP values were between 5 and 7, and the environment was very favorable for significant tornadoes (Fig. 15).

The environment east of the boundary continued to grow more volatile with time as the simulated supercell approached the boundary. At 2000 UTC, when the supercell was just east of the boundary (Fig. 16), SBCAPE values in excess of 3000 J kg^{-1} were present in the inflow region of the supercell (Fig. 16a). Additionally, 0–1-km SRH values in excess of 500 m^2 s^{-2} were present in the inflow region of the supercell (Fig. 16d), highlighting the very intense low-level wind shear and inferred streamwise vorticity east of the boundary. At this time, the supercell was undoubtedly having an impact on the environment and contributing to the very large values of 0–1-km SRH. Low-level inflow accelerations in the vicinity of supercell thunderstorms have been shown to increase low-level wind shear (e.g., Nowotarski and Markowski 2016; Parker 2014). The values at 1900 UTC were therefore likely more representative of the near-storm environment as the supercell crossed the boundary. The impact of this environment on the intensity and evolution of the simulated supercell is discussed in the following section.

4. Storm-scale characteristics

The simulated supercell interacted with the boundary between 1930 and 2000 UTC and underwent substantial structural changes during and after the interaction, as is summarized in Fig. 17. Prior to the boundary interaction (before 1930 UTC), the supercell was in a quasi-steady state, as illustrated in Fig. 17d. During this period, the maximum 1 and 5 km AGL updraft speed and maximum 1 and 5 km AGL vertical vorticity, while variable, did not show any large, overall trend. The supercell began to interact with the boundary at approximately 1937 UTC, when the low-level updraft began to overlap with the narrow axis of largest instability and southeasterly flow to the east of the boundary (Fig. 18). About 15–20 min thereafter, the maximum updraft speed and maximum vertical vorticity at both 1 and 5 km increased, indicative of the intensification of the supercell. The most pronounced increase occurred in the 5-km vertical vorticity, suggesting that the midlevel mesocyclone strengthened rapidly after crossing the boundary (red, dashed line in Fig. 17d). This increase in midlevel rotation followed an increase in the 5-km updraft speed (blue, dashed line in Fig. 17d). The increased difference between the 5-km updraft speed and 1-km updraft speed (blue, solid line in Fig. 17d), centered around 2000 UTC, implies the presence of enhanced stretching of vertical vorticity during this period. The simulated reflectivity structure of the supercell exhibited a more classic appearance after the interaction with the boundary, as the cell increased in size, featured higher reflectivity, and was characterized by a more defined hook echo (Figs. 17a–c). In the simulation, the maximum 5-km vertical vorticity decreased between 2010 and 2020 UTC, as the mesocyclone became more occluded (not shown).

To further study the role of the boundary in the intensification of the supercell, back trajectories were calculated utilizing LAGRANTO for parcels seeded at both 5 and 2 km MSL height within the updraft core (chosen to be $w > 10$ m s^{-1} at 5 km and $w > 5$ m s^{-1} at 2 km) at both 1945 UTC and 2000 UTC (Fig. 19). As before, the back trajectories were calculated using 1-min WRF output and a 6-s trajectory integration time step. We tested the sensitivity of the back trajectories to smaller trajectory integration time steps, but the results were similar. Gray and Frame (2019) similarly

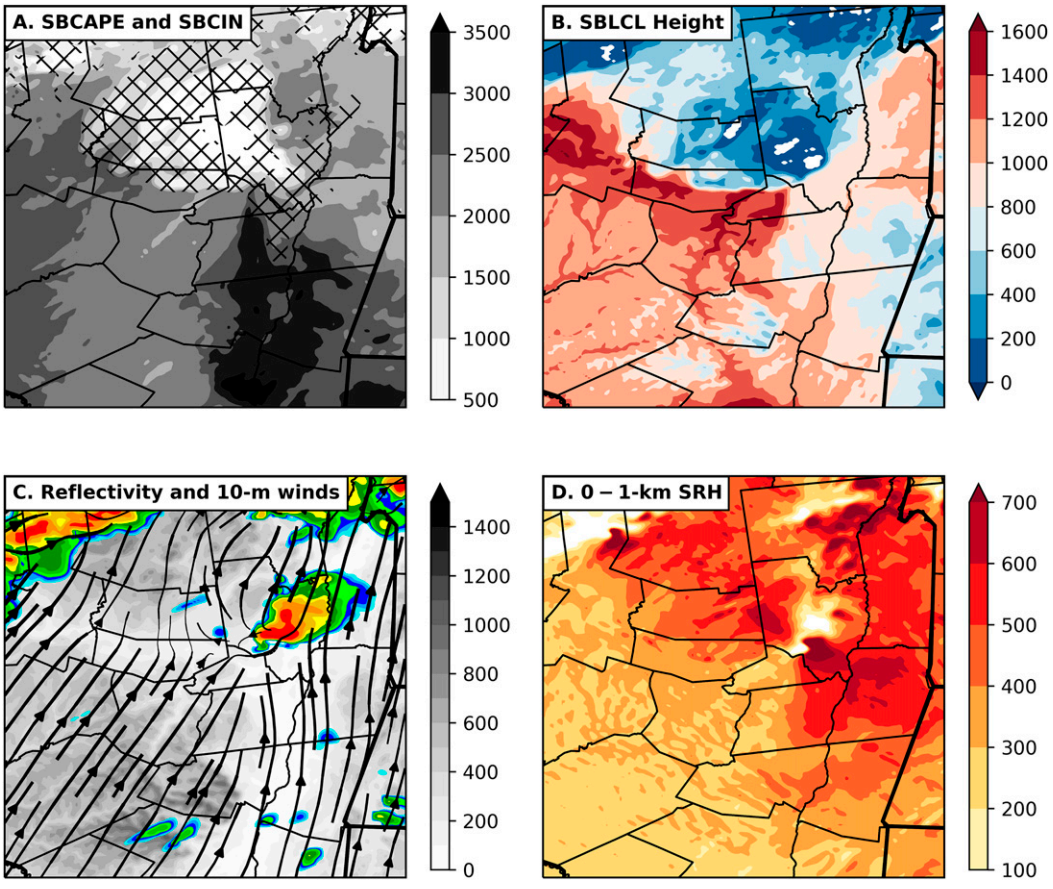

FIG. 16. As in Fig. 13, but for 2000 UTC.

used trajectories to assess the source regions of air within supercell updrafts based on 1-km horizontal grid spacing WRF output. They calculated the trajectories using 2-min WRF output with a trajectory time step of 1 min. Therefore, the time step utilized here should be sufficient to examine supercell inflow. These back trajectories all have endpoints at 1900 UTC. Hereafter, the back trajectory endpoints will be referred to as the initial locations or origins of the updraft air parcels. Only trajectories with initial elevations less than 2000 m MSL are discussed here, to focus on the low-level inflow.

The low-level back trajectories from both the mid- and low-level updrafts at 1945 UTC indicate that the source region of air in the updraft at that time was primarily from west of the boundary (Figs. 19a,c). A small number of the 2-km updraft trajectories at 1945 UTC did originate from the low elevations in Schenectady and Albany County at 1900 UTC. These parcel locations are east of the boundary, suggesting the boundary interaction had just started at this time (Fig. 18).

The back trajectories from both the mid- and low-level updrafts at 2000 UTC suggest a change in predominant source region was underway (Figs. 19b,d). A greater proportion of the parcels within the mid- and low-level updrafts at 2000 UTC had initial locations to the east of the boundary. This change suggests that, at 2000 UTC, the inflow into the supercell was characterized by an increase in SBCAPE and 0–1-km SRH, associated with the more volatile environment east of the boundary (Fig. 16). The time of 2000 UTC is near the time that the low- and midlevel updraft speeds and the low-level vertical vorticity reached a maximum. Therefore, the partial change in the source region of the low-level inflow corresponded with the intensification of the simulated supercell between 1945 and 2000 UTC.

To isolate changes in the low-level inflow, Fig. 20a depicts the initial height and θ_e of parcels that were located within the 5-km updraft core at 1945 UTC and 2000 UTC. At 1945 UTC, the parcels that entered the updraft and originated at 1900 UTC between 400 and 1000 m AGL had θ_e values mostly near 340 K. At 2000 UTC, inflow parcels originating at 1900 UTC between 400 and 1000 m AGL had θ_e values mostly near 342 K. This difference captures the increase in low-level θ_e, and inferred low-level buoyancy, in the supercell inflow as the supercell moved across the boundary.

Similarly, Fig. 20b depicts the streamwise vorticity at 1900 UTC for the parcels that were ingested into the 5-km updraft core at 1945 UTC and 2000 UTC. The source values of streamwise vorticity at 1900 UTC are substantially larger for parcels in the

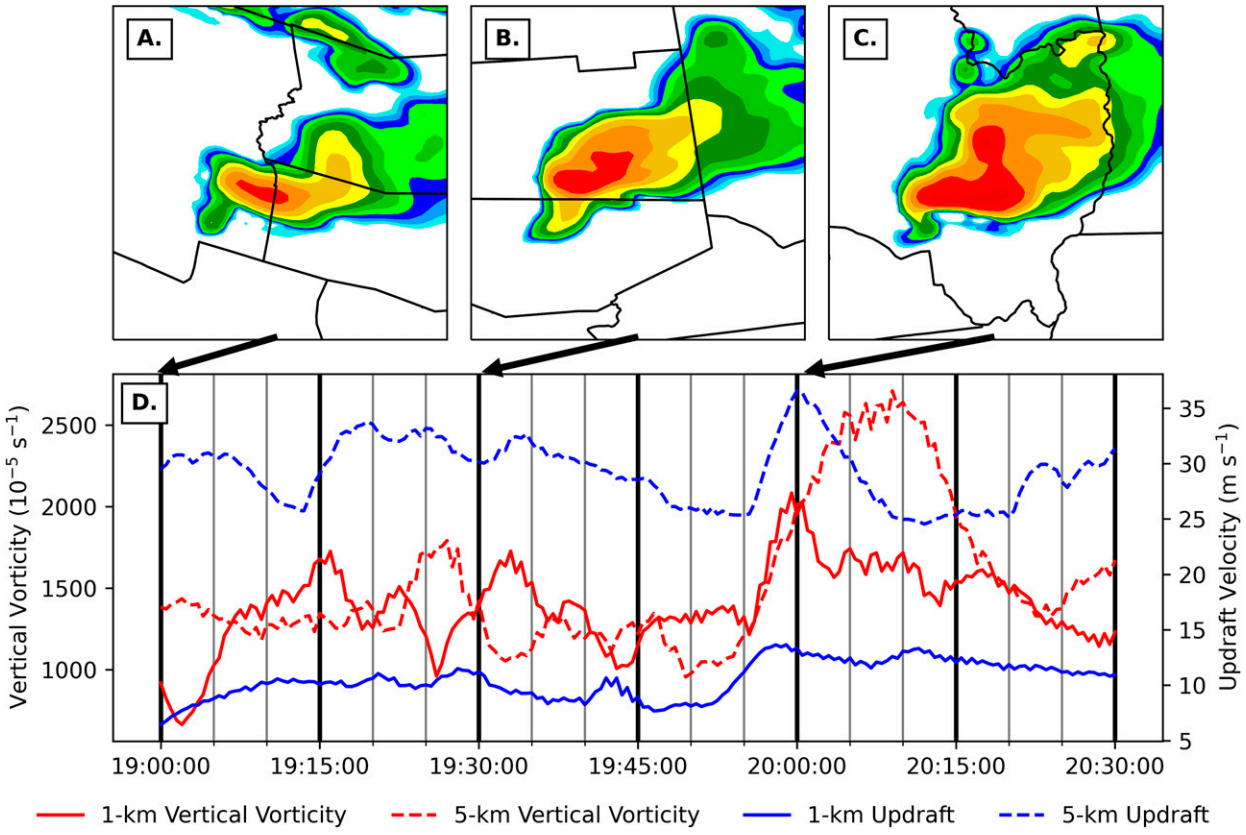

FIG. 17. 1-km AGL reflectivity (dBZ; color following Fig. 6) for the simulated supercell at (a) 1900, (b) 1930, and (c) 2000 UTC. (d) A time series of the maximum 1 km AGL updraft (blue, solid), the maximum 5 km AGL updraft (blue, dashed), the maximum 1 km AGL vertical vorticity (red, solid), and the maximum 5 km AGL vertical vorticity (red, dashed).

5-km updraft core at 2000 UTC (8×10^{-3}–15×10^{-3} s^{-1}) than for parcels in the 5-km updraft core at 1945 UTC (around 5×10^{-3} s^{-1}). Markowski et al. (2003) found that the mean environment for significantly tornadic supercells is typically characterized by streamwise vorticity of larger than 8×10^{-3} s^{-1} below 1 km AGL. Therefore, the values of streamwise vorticity ingested into the updraft at 2000 UTC are consistent with values associated with significant tornado environments. The tilting and stretching of this streamwise vorticity are implied along the trajectory paths presented in Fig. 19, and therefore the environment east of the boundary supported the strong low-level updraft and low-level rotation in the simulated thunderstorm around 2000 UTC (Fig. 17d; Peters et al. 2020).

It is important to recognize that vorticity generation along the forward flank horizontal buoyancy gradient and thunderstorm outflow can also be an important contributor to the strength of the low-level mesocyclone and tornadogenesis process (e.g., Rotunno and Klemp 1985; Dahl et al. 2014; Markowski and Richardson 2009). It is additionally important to note that the simulation here does not resolve tornado-scale processes. However, evidence of the ingestion of increasingly buoyant air parcels characterized by large streamwise vorticity, combined with the intensification of the simulated supercell noted in Fig. 17, supports the hypothesis that tornadogenesis was favored east of the boundary.

5. Discussion

The results clearly suggest that terrain channeling of low-level winds can result in the formation of a mesoscale boundary at the intersection of the Mohawk and Hudson valleys, and that this boundary can have an impact on the occurrence of severe weather. This result is consistent with previous research that has indicated that mesoscale boundaries can play a role in tornadogenesis (e.g., Maddox et al. 1980; Markowski et al. 1998; Markowski and Richardson 2009). The simulated boundary augmented the SRH to the east of the boundary (Fig. 13d; Rasmussen et al. 2000), and the ''cool'' side of the boundary acted as a source of streamwise vorticity favoring tornadogenesis in that region (Fig. 20b; Atkins et al. 1999). The unique aspect here is that the boundary herein is terrain induced, rather than being a synoptic-scale or storm-outflow feature.

Interestingly, the boundary documented here has properties that are consistent with drylines. The vertical structure of the boundary closely matches observations and the conceptual

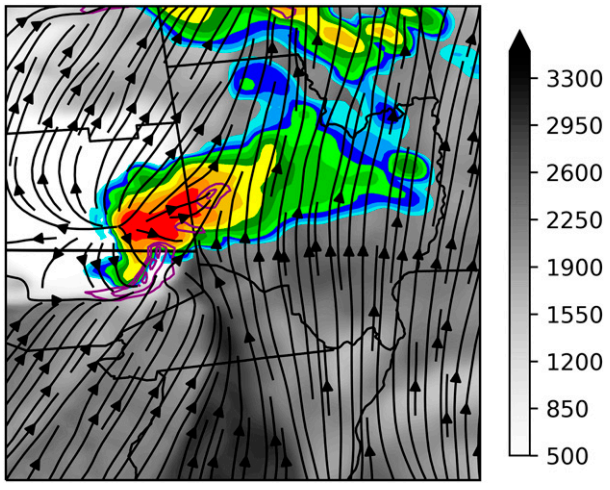

FIG. 18. At 1937 UTC, the simulated 1 km AGL reflectivity (dBZ; color following Fig. 6), 10-m wind streamlines, 1 km AGL vertical motion (purple contours; every 5 m s^{-1} starting at 5 m s^{-1}), and SBCAPE (J kg^{-1}).

model of dryline structure (Parsons et al. 1991; Weckwerth and Parsons 2006; Wakimoto and Murphey 2009), with a steep leading edge to the cool, moist air mass and a narrow updraft on the warm, dry side of the boundary. There are, however, important distinctions between the boundary documented here and typical synoptic-scale drylines. First, the dewpoint difference across the boundary is an order of magnitude smaller than for synoptic-scale drylines observed in the Great Plains of the United States (e.g., Parsons et al. 1991). Because of the smaller moisture gradient, severe convection was supported on both sides of the simulated mesoscale boundary. Additionally, the movement of synoptic-scale drylines is often governed by the diurnal processes in the boundary layer along with the slope of terrain (Parsons et al. 1991). The possibility exists that these processes also played a role in the development of the boundary in this case. However, in this case, the location of the boundary is linked to major terrain features and the critical role of terrain channeling.

Similar terrain-induced boundaries have been observed in additional cases in upstate New York. Tang et al. (2016) documented a north-south oriented boundary within the Hudson and Mohawk valleys on 22 May 2014, and this boundary was hypothesized to play a role in the Duanesburg tornado. Another similar boundary occurred on 31 May 2017. In that case, a strong moisture gradient and wind shift was directly observed within the Mohawk Valley near the intersection with the Hudson Valley by the New York State Mesonet (Fig. 21). Surface dewpoint differences exceeded 12°F (6.7°C) across the boundary within the Mohawk Valley. A cluster of thunderstorms rapidly intensified after interacting with the boundary and resulted in a concentration of severe wind and hail reports east of the boundary (NOAA 2020).

While the results here suggest that a terrain-driven boundary played an important role in the formation of the Mechanicville tornado, it is possible that the merger between the supercell and a squall line impacted the tornadogenesis process as well. As presented in LaPenta et al. (2005), the storm that produced the Mechanicville tornado developed over 50 km ahead of a squall line to the west. Just prior to tornadogenesis, this advancing squall line began to merge with the leading supercell (Fig. 5c). The reader is referred to LaPenta et al. (2005) for a more thorough description and radar analysis of the supercell–squall line merger. This merger was not present in the simulation, which allowed for a focus on the role of terrain and the supercell–boundary interaction. However, the supercell–squall line merger might have contributed to the formation of the Mechanicville tornado in actuality. Significant tornadoes have been documented after similar storm mergers (e.g., Goodman and Knupp 1993; Wolf 1998). Bosart et al. (2006) found that the Great Barrington, Massachusetts tornado developed after complex storm-scale interactions. In agreement with these case analyses, French and Parker (2014) demonstrated using idealized simulations that the potential for severe weather is enhanced near storm merger locations. French and Parker (2012) analyzed a set of 21 cases in which isolated supercells merged with squall lines and found that storm mergers may in some way serve as instigators for tornado formation in environments favorable for tornadoes. However, for strongly forced events like the 31 May 1998 event, they found that tornadoes were less common during and after the merger. Additionally, it was found that tornadoes that occurred after the merger were generally weaker and had shorter pathlengths than those that occurred with isolated supercells. Therefore, the Mechanicville tornado may potentially be an unusually strong, long-lived, postmerger tornado.

It has been observed that other terrain features drive similar mesoscale boundaries that provide a focus for severe convection. One prominent example is the Denver convergence vorticity zone (DCVZ) and Denver Cyclone, which have been found to impact the occurrence and severity of convection in Colorado (Szoke et al. 1984). Childs and Schumacher (2019) found a local maximum in tornado reports in the region of the DCVZ. Outside of the United States, Pistotnik et al. (2011) documented a ''dryline-like boundary'' during a severe weather event in Austria that developed as a result of subsidence on the north side of the Alps. It is possible that similar boundaries may exist near other prominent terrain features, including river valley intersections. Tornadoes have been documented in several additional regions of complex topography in the United States, including the Rocky Mountains in Colorado (Bluestein 2000; Nuss 1986), the Southern Cumberland System in Alabama, Georgia, and Tennessee (Lyza and Knupp 2018; Lyza et al. 2020), the Sacramento Valley (Braun and Monteverdi 1991), the Los Angeles Basin (Hales 1985), California (Blier and Batten 1994), and the Teton–Yellowstone Wilderness in Wyoming (Fujita 1989). In the southeastern United States, there is considerable overlap between regions of substantial tornado risk and regions of complex topography (Coleman and Dixon 2014). Therefore, mechanisms through which terrain can modulate the potential for severe convection in one region, such as the northeastern United States, may be

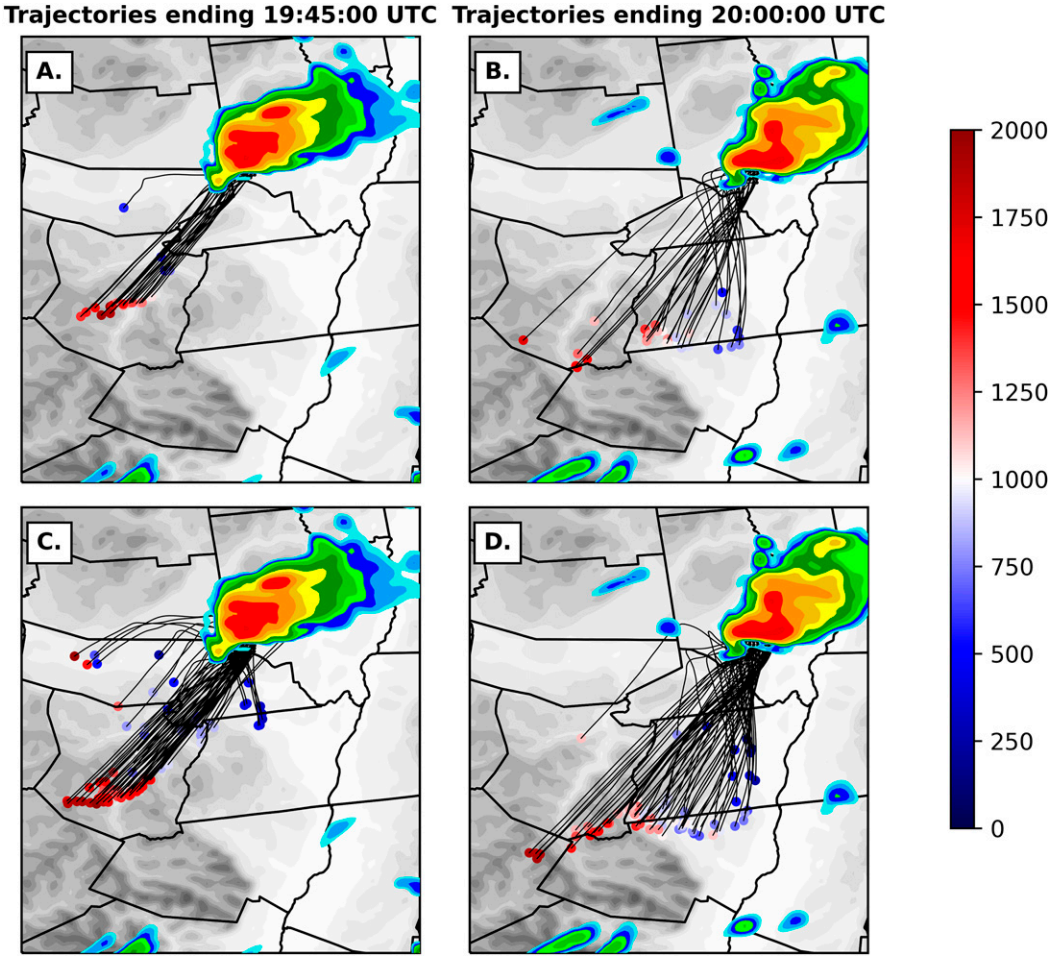

FIG. 19. Back trajectories seeded (a) at 1945 UTC within the 5 km MSL updraft core, (b) at 2000 UTC within the 5 km MSL updraft core, (c) at 1945 UTC within the 2 km MSL updraft core, and (d) at 2000 UTC within the 2 km MSL updraft core. The colored dots indicate the 1900 UTC location and height (m MSL; shaded) of the trajectories. The 1 km AGL reflectivity (dBZ) and terrain height (m) are shaded following Fig. 6.

applicable to severe thunderstorm events in different regions both within the United States and globally.

6. Conclusions

The Mechanicville tornado of 31 May 1998 was a rare, high-impact tornado that occurred in the northeastern United States. A high-resolution WRF Model simulation of the 31 May 1998 event suggests that a robust mesobeta-scale boundary developed at the intersection of the Hudson and Mohawk valleys. The properties of the boundary resemble those of a dryline. The boundary was characterized by a moisture gradient, with dewpoint values in excess of 20°–21°C to the east of the boundary within the Hudson Valley. Additionally, consistent with dryline structure, there was a layer of enhanced stability around 1 km AGL to the east of the boundary. A similar stable layer was observed by the 1800 UTC Albany upper-air sounding. Finally, there were strong, south-southeasterly winds near the surface to the east of the boundary within the Hudson Valley, while winds to the west within the Mohawk Valley were south-southwesterly. Terrain channeling played a crucial role in the development of this boundary. Trajectories indicate that confluence in the wake of the high terrain features in the Catskill Mountains supported the tightening of the boundary in the region at the intersection of the Mohawk and Hudson valleys.

Although a large area of the northeastern United States was characterized by an environment favorable for severe convection, the region along and immediately east of the boundary, in the vicinity of Mechanicville, was characterized by enhanced instability, low-level wind shear, and SRH. The southerly and south-southeasterly surface winds in the Hudson Valley resulted in substantial hodograph curvature in the lowest 1 km AGL, supporting 0–1-km SRH near the 90th percentile of model proximity soundings ahead of significantly tornadic supercells

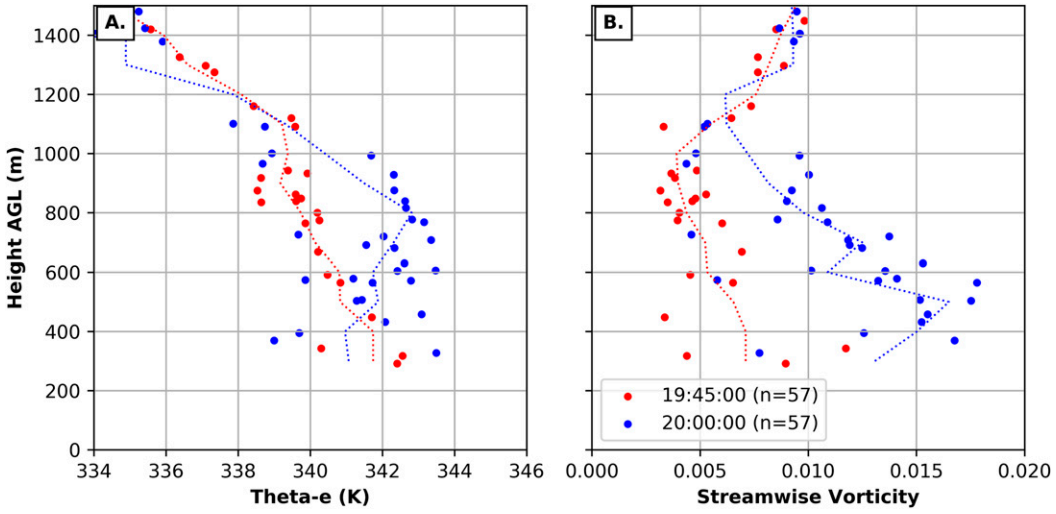

FIG. 20. The 1900 UTC height (m AGL) and (a) θ_e (K) and (b). streamwise vorticity (s^{-1}) for parcels that were ingested into the midlevel (5 km) updraft core at 1945 (red) and 2000 UTC (blue). The dashed line indicates a 4-nearest-neighbors line fit to the points.

(Thompson et al. 2007). As a result, the storm environment in this region was extremely favorable for tornadogenesis. A simulated supercell intensified within 20 min after crossing the boundary and entering the volatile environment within the Hudson Valley. Trajectories indicate that the period of intensification occurred as high θ_e and high streamwise vorticity air was ingested into the supercell updraft from the region to the east of the boundary.

The presence of similar boundaries in several severe thunderstorm cases in New York suggests that mesoscale boundaries that develop as a result of terrain channeling may play an important role in modulating the local severe thunderstorm environment of the region at the intersection of the Mohawk and Hudson valleys. The New York State Mesonet, along with high-resolution models and analyses, will allow these boundaries to be observed better in real time. The recognition of these boundaries in advance may be useful in increasing situational awareness of where the risk of severe weather may be locally higher during severe weather events. Additional research would be useful to establish a climatology of these boundaries, to identify the sensitivity of boundary formation to small-scale terrain features, and to extend the investigation to additional severe weather events.

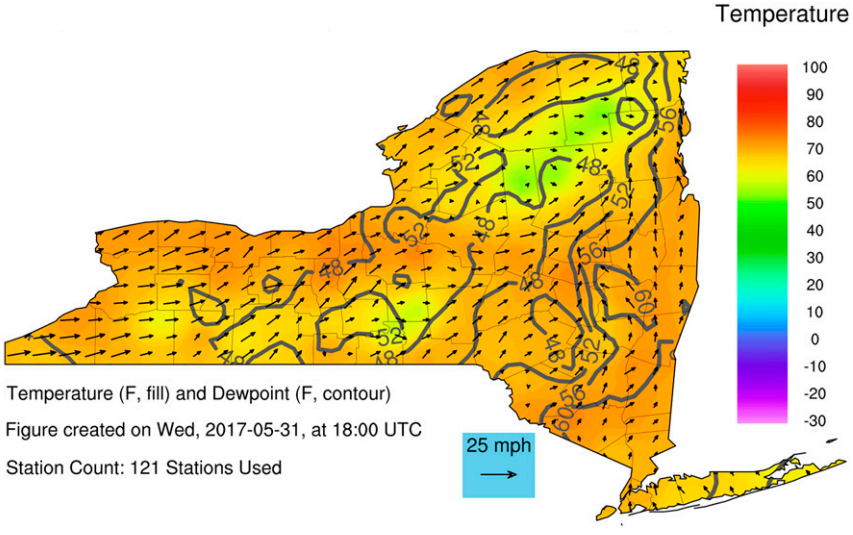

FIG. 21. The 2-m temperature (fill; °F), 2-m dewpoint (°F; contours every 4°F), and 10-m winds (vectors) at 1800 UTC 31 May 2017, interpolated from the New York State Mesonet station data. This product is available in real time at Bassill (2020).

Acknowledgments. We thank three anonymous reviewers for their insightful comments that improved this manuscript. The research was funded by NOAA Collaborative Science, Technology, and Applied Research Program Grant NA19NWS4680006. The MetPy, WRF-Python, and Python ARM Radar Toolkit Python packages were utilized in the analysis and production of figures.

Data availability statement. Radar data are available from NOAA National Centers for Environmental Information (doi:10.7289/V5W9574V). NARR data and surface observations are also available through the NOAA NCEI. Upper-air sounding data are available through the University of Wyoming upper-air archive (http://weather.uwyo.edu/upperair/sounding.html). Tornado reports are available through the NOAA National Weather Service Storm Prediction Center Severe Weather Database (https://www.spc.noaa.gov/wcm/#data). WRF Model output is available upon request.

REFERENCES

Atkins, N. T., M. L. Weisman, and L. J. Wicker, 1999: The influence of preexisting boundaries on supercell evolution. *Mon. Wea. Rev.*, **127**, 2910–2927, https://doi.org/10.1175/1520-0493(1999)127<2910:TIOPBO>2.0.CO;2.

Bassill, N., 2020: NYS Mesonet Products. New York State Mesonet, accessed 28 March 2020, https://operations.nysmesonet.org/~nbassill/.

Benjamin, S. G., and Coauthors, 2016: A North American hourly assimilation and model forecast cycle: The Rapid Refresh. *Mon. Wea. Rev.*, **144**, 1669–1694, https://doi.org/10.1175/MWR-D-15-0242.1.

Blier, W., and K. A. Batten, 1994: On the incidence of tornadoes in California. *Wea. Forecasting*, **9**, 301–315, https://doi.org/10.1175/1520-0434(1994)009<0301:OTIOTI>2.0.CO;2.

Bluestein, H. B., 2000: A tornadic supercell over elevated, complex terrain: The Divide, Colorado, storm of 12 July 1996. *Mon. Wea. Rev.*, **128**, 795–809, https://doi.org/10.1175/1520-0493(2000)128<0795:ATSOEC>2.0.CO;2.

Bosart, L. F., A. Seimon, K. D. LaPenta, and M. J. Dickinson, 2006: Supercell tornadogenesis over complex terrain: The Great Barrington, Massachusetts, tornado on 29 May 1995. *Wea. Forecasting*, **21**, 897–922, https://doi.org/10.1175/WAF957.1.

Braun, S. A., and J. P. Monteverdi, 1991: An analysis of a mesocyclone-induced tornado occurrence in northern California. *Wea. Forecasting*, **6**, 13–31, https://doi.org/10.1175/1520-0434(1991)006<0013:AAOAMT>2.0.CO;2.

Chen, F., and J. Dudhia, 2001: Coupling an advanced land surface-hydrology model with the Penn State–NCAR MM5 modeling system. Part I: Model implementation and sensitivity. *Mon. Wea. Rev.*, **129**, 569–585, https://doi.org/10.1175/1520-0493(2001)129<0569:CAALSH>2.0.CO;2.

Childs, S. J., and R. S. Schumacher, 2019: An updated severe hail and tornado climatology for eastern Colorado. *J. Appl. Meteor. Climatol.*, **58**, 2273–2293, https://doi.org/10.1175/JAMC-D-19-0098.1.

Coffer, B. E., and M. D. Parker, 2017: Simulated supercells in nontornadic and tornadic VORTEX2 environments. *Mon. Wea. Rev.*, **145**, 149–180, https://doi.org/10.1175/MWR-D-16-0226.1.

——, and ——, 2018: Is there a ''tipping point'' between simulated nontornadic and tornadic supercells in VORTEX2 environments? *Mon. Wea. Rev.*, **146**, 2667–2693, https://doi.org/10.1175/MWR-D-18-0050.1.

——, ——, J. M. L. Dahl, L. J. Wicker, and A. J. Clark, 2017: Volatility of tornadogenesis: An ensemble of simulated nontornadic and tornadic supercells in VORTEX2 environments. *Mon. Wea. Rev.*, **145**, 4605–4625, https://doi.org/10.1175/MWR-D-17-0152.1.

——, ——, R. L. Thompson, B. T. Smith, and R. E. Jewell, 2019: Using near-ground storm relative helicity in supercell tornado forecasting. *Wea. Forecasting*, **34**, 1417–1435, https://doi.org/10.1175/WAF-D-19-0115.1.

Coleman, T. A., and P. G. Dixon, 2014: An objective analysis of tornado risk in the United States. *Wea. Forecasting*, **29**, 366–376, https://doi.org/10.1175/WAF-D-13-00057.1.

Dahl, J. M. L., M. D. Parker, and L. J. Wicker, 2014: Imported and storm-generated near-ground vertical vorticity in a simulated supercell. *J. Atmos. Sci.*, **71**, 3027–3051, https://doi.org/10.1175/JAS-D-13-0123.1.

Davies-Jones, R., 1984: Streamwise vorticity: The origin of updraft rotation in supercell storms. *J. Atmos. Sci.*, **41**, 2991–3006, https://doi.org/10.1175/1520-0469(1984)041<2991:SVTOOU>2.0.CO;2.

——, 2015: A review of supercell and tornado dynamics. *Atmos. Res.*, **158–159**, 274–291, https://doi.org/10.1016/j.atmosres.2014.04.007.

Esterheld, J. M., and D. J. Giuliano, 2008: Discriminating between tornadic and non-tornadic supercells: A new hodograph technique. *Electron. J. Severe Storms Meteor.*, **3** (2), https://ejssm.org/archives/2008/vol-3-2-2008/.

European Centre for Medium-Range Weather Forecasts, 2017: ERA5 reanalysis. National Center for Atmospheric Research, Computational and Information Systems Laboratory, accessed 6 July 2020, https://doi.org/10.5065/D6X34W69.

French, A. J., and M. D. Parker, 2012: Observations of mergers between squall lines and isolated supercell thunderstorms. *Wea. Forecasting*, **27**, 255–278, https://doi.org/10.1175/WAF-D-11-00058.1.

——, and ——, 2014: Numerical simulations of bow echo formation following a squall line-supercell merger. *Mon. Wea. Rev.*, **142**, 4791–4822, https://doi.org/10.1175/MWR-D-13-00356.1.

Fujita, T. T., 1989: The Teton–Yellowstone tornado of 21 July 1987. *Mon. Wea. Rev.*, **117**, 1913–1940, https://doi.org/10.1175/1520-0493(1989)117<1913:TTYTOJ>2.0.CO;2.

Geerts, B., T. Andretta, S. J. Luberda, J. Vogt, Y. Wang, L. D. Oolman, J. Finch, and D. Bikos, 2009: A case study of a long-lived tornadic mesocyclone in a low-CAPE complex-terrain environment. *Electron. J. Severe Storms Meteor.*, **4** (3), https://ejssm.org/archives/2009/vol-4-3-2009/.

Goodman, S. J., and K. R. Knupp, 1993: Tornadogenesis via squall line and supercell interaction: The November 15, 1989, Huntsville, Alabama, tornado. *The Tornado: Its Structure, Dynamics, Prediction, and Hazards, Geophys. Monogr.*, Vol. 79, Amer. Geophys. Union, 183–200.

Gray, K., and J. Frame, 2019: Investigating the transition from elevated multicellular convection to surface-based supercells during the tornado outbreak of 24 August 2016 using a WRF Model simulation. *Wea. Forecasting*, **34**, 1051–1079, https://doi.org/10.1175/WAF-D-18-0209.1.

Grell, G. A., and S. R. Freitas, 2014: A scale and aerosol aware stochastic convective parameterization for weather and air quality modeling. *Atmos. Chem. Phys.*, **14**, 5233–5250, https://doi.org/10.5194/acp-14-5233-2014.

Hales, J. E., Jr., 1985: Synoptic features associated with Los Angeles tornado occurrences. *Bull. Amer. Meteor. Soc.*, **66**, 657–662, https://doi.org/10.1175/1520-0477-66.6.657.

Hannesen, R., N. Dotzek, H. Gysi, and K. D. Beheng, 1998: Case study of a tornado in the upper Rhine Valley. *Meteor. Z.*, **7**, 163–170, https://doi.org/10.1127/metz/7/1998/163.

Hill, A. J., C. C. Weiss, and B. C. Ancell, 2016: Ensemble sensitivity analysis for mesoscale forecasts of dryline convection initiation. *Mon. Wea. Rev.*, **144**, 4161–4182, https://doi.org/10.1175/MWR-D-15-0338.1.

Homar, V., M. Gayá, R. Romero, C. Ramis, and S. Alonso, 2003: Tornadoes over complex terrain: An analysis of the 28th August 1999 tornadic event in eastern Spain. *Atmos. Res.*, **67–68**, 301–317, https://doi.org/10.1016/S0169-8095(03)00064-4.

Iacono, M. J., J. S. Delamere, E. J. Mlawer, M. W. Shephard, S. A. Clough, and W. D. Collins, 2008: Radiative forcing by long-lived greenhouse gases: Calculations with the AER radiative transfer models. *J. Geophys. Res.*, **113**, D13103, https://doi.org/10.1029/2008JD009944.

Katona, B., P. Markowski, C. Alexander, and S. Benjamin, 2016: The influence of topography on convective storm environments in the eastern United States as deduced from the HRRR. *Wea. Forecasting*, **31**, 1481–1490, https://doi.org/10.1175/WAF-D-16-0038.1.

Kovacs, M., and D. J. Kirshbaum, 2016: Topographic impacts on the spatial distribution of deep convection over southern Quebec. *J. Appl. Meteor. Climatol.*, **55**, 743–762, https://doi.org/10.1175/JAMC-D-15-0239.1.

LaPenta, K. D., L. F. Bosart, T. J. Galarneau Jr., and M. J. Dickinson, 2005: A multiscale examination of the 31 May 1998 Mechanicville, New York, tornado. *Wea. Forecasting*, **20**, 494–516, https://doi.org/10.1175/WAF875.1.

Lyza, A. W., and K. R. Knupp, 2018: A background investigation of tornado activity across the southern Cumberland Plateau terrain system of northeastern Alabama. *Mon. Wea. Rev.*, **146**, 4261–4278, https://doi.org/10.1175/MWR-D-18-0300.1.

——, T. A. Murphy, B. T. Goudeau, P. T. Pangle, K. R. Knupp, and R. A. Wade, 2020: Observed near-storm environment variations across the southern Cumberland Plateau system in northeastern Alabama. *Mon. Wea. Rev.*, **148**, 1465–1482, https://doi.org/10.1175/MWR-D-19-0190.1.

Maddox, R. A., L. R. Hoxit, and C. F. Chappell, 1980: A study of tornadic thunderstorm interactions with thermal boundaries. *Mon. Wea. Rev.*, **108**, 322–336, https://doi.org/10.1175/1520-0493(1980)108<0322:ASOTTI>2.0.CO;2.

Markowski, P. M., and Y. P. Richardson, 2009: Tornadogenesis: Our current understanding, forecasting considerations, and questions to guide future research. *Atmos. Res.*, **93**, 3–10, https://doi.org/10.1016/j.atmosres.2008.09.015.

——, and N. Dotzek, 2011: A numerical study of the effects of orography on supercells. *Atmos. Res.*, **100**, 457–478, https://doi.org/10.1016/j.atmosres.2010.12.027.

——, E. N. Rasmussen, and J. M. Straka, 1998: The occurrence of tornadoes in supercells interacting with boundaries during VORTEX-95. *Wea. Forecasting*, **13**, 852–859, https://doi.org/10.1175/1520-0434(1998)013<0852:TOOTIS>2.0.CO;2.

——, C. Hannon, J. Frame, E. Lancaster, A. Pietrycha, R. Edwards, and R. L. Thompson, 2003: Characteristics of vertical wind profiles near supercells obtained from the Rapid Update Cycle. *Wea. Forecasting*, **18**, 1262–1272, https://doi.org/10.1175/1520-0434(2003)018<1262:COVWPN>2.0.CO;2.

Martin, W. J., and M. Xue, 2006: Sensitivity analysis of convection of the 24 May 2002 IHOP case using very large ensembles. *Mon. Wea. Rev.*, **134**, 192–207, https://doi.org/10.1175/MWR3061.1.

Mesinger, F., and Coauthors, 2006: North American Regional Reanalysis. *Bull. Amer. Meteor. Soc.*, **87**, 343–360, https://doi.org/10.1175/BAMS-87-3-343.

Nakanishi, M., and H. Niino, 2006: An improved Mellor–Yamada level-3 model: Its numerical stability and application to a regional prediction of advection fog. *Bound.-Layer Meteor.*, **119**, 397–407, https://doi.org/10.1007/s10546-005-9030-8.

NOAA, 2020: Storm events database. NOAA, accessed 29 July 2020, https://www.ncdc.noaa.gov/stormevents/.

Nowotarski, C. J., and P. M. Markowski, 2016: Modifications to the near-storm environment induced by simulated supercell thunderstorms. *Mon. Wea. Rev.*, **144**, 273–293, https://doi.org/10.1175/MWR-D-15-0247.1.

——, ——, and Y. P. Richardson, 2011: The characteristics of numerically simulated supercell storms situated over statically stable boundary layers. *Mon. Wea. Rev.*, **139**, 3139–3162, https://doi.org/10.1175/MWR-D-10-05087.1.

Nuss, W. A., 1986: Observations of a mountain tornado. *Mon. Wea. Rev.*, **114**, 233–237, https://doi.org/10.1175/1520-0493(1986)114<0233:OOAMT>2.0.CO;2.

Parker, M. D., 2014: Composite VORTEX2 supercell environments from near-storm soundings. *Mon. Wea. Rev.*, **142**, 508–529, https://doi.org/10.1175/MWR-D-13-00167.1.

Parsons, D. B., M. A. Shapiro, R. M. Hardesty, R. J. Zamora, and J. M. Intrieri, 1991: The finescale structure of a west Texas dryline. *Mon. Wea. Rev.*, **119**, 1242–1258, https://doi.org/10.1175/1520-0493(1991)119<1242:TFSOAW>2.0.CO;2.

Peters, J. M., C. J. Nowotarski, J. P. Mulholland, and R. L. Thompson, 2020: The influences of effective inflow layer streamwise vorticity and storm-relative flow on supercell updraft properties. *J. Atmos. Sci.*, **77**, 3033–3057, https://doi.org/10.1175/JAS-D-19-0355.1.

Pistotnik, G., A. Martin Holzer, R. Kaltenböck, and S. Tschannett, 2011: An F3 downburst in Austria—A case study with special focus on the importance of real-time site surveys. *Atmos. Res.*, **100**, 565–579, https://doi.org/10.1016/j.atmosres.2010.10.011.

Rasmussen, E. N., and D. O. Blanchard, 1998: A baseline climatology of sounding-derived supercell and tornado forecast parameters. *Wea. Forecasting*, **13**, 1148–1164, https://doi.org/10.1175/1520-0434(1998)013<1148:ABCOSD>2.0.CO;2.

——, S. Richardson, J. M. Straka, P. M. Markowski, and D. O. Blanchard, 2000: The association of significant tornadoes with a baroclinic boundary on 2 June 1995. *Mon. Wea. Rev.*, **128**, 174–191, https://doi.org/10.1175/1520-0493(2000)128<0174:TAOSTW>2.0.CO;2.

Rogers, J., P. Marsh, and R. Thompson, 2021: Sounding climatology page. NOAA/Storm Prediction Center, accessed 2 February 2021, http://www.spc.noaa.gov/exper/soundingclimo/.

Rotunno, R., and J. Klemp, 1985: On the rotation and propagation of simulated supercell thunderstorms. *J. Atmos. Sci.*, **42**, 271–292, https://doi.org/10.1175/1520-0469(1985)042<0271:OTRAPO>2.0.CO;2.

Skamarock, W. C., and Coauthors, 2008: A description of the Advanced Research WRF version 3. NCAR Tech. Note NCAR/TN-475+STR, 113 pp., https://doi.org/10.5065/D68S4MVH.

Sprenger, M., and H. Wernli, 2015: The LAGRANTO Lagrangian analysis tool— version 2.0. *Geosci. Model. Dev.*, **8**, 2569–2586, https://doi.org/10.5194/gmd-8-2569-2015.

Szoke, E. J., M. L. Weisman, J. M. Brown, F. Caracena, and T. W. Schlatter, 1984: A subsynoptic analysis of the Denver tornadoes of 3 June 1981. *Mon. Wea. Rev.*, **112**, 790–808, https://doi.org/10.1175/1520-0493(1984)112<0790:ASAOTD>2.0.CO;2.

Tang, B., M. Vaughan, R. Lazear, K. Corbosiero, L. Bosart, T. Wasula, I. Lee, and K. Lipton, 2016: Topographic and boundary influences on the 22 May 2014 Duanesburg, New York, tornadic supercell. *Wea. Forecasting*, **31**, 107–127, https://doi.org/10.1175/WAF-D-15-0101.1.

Thompson, G., and T. Eidhammer, 2014: A study of aerosol impacts on clouds and precipitation development in a large winter cyclone. *J. Atmos. Sci.*, **71**, 3636–3658, https://doi.org/10.1175/JAS-D-13-0305.1.

Thompson, R. L., R. Edwards, J. A. Hart, K. L. Elmore, and P. Markowski, 2003: Close proximity soundings within supercell environments obtained from the Rapid Update Cycle. *Wea. Forecasting*, **18**, 1243–1261, https://doi.org/10.1175/1520-0434(2003)018<1243:CPSWSE>2.0.CO;2.

——, C. M. Mead, and R. Edwards, 2007: Effective storm-relative helicity and bulk shear in supercell thunderstorm environments. *Wea. Forecasting*, **22**, 102–115, https://doi.org/10.1175/WAF969.1.

——, B. T. Smith, J. S. Grams, A. R. Dean, and C. Broyles, 2012: Convective modes for significant severe thunderstorms in the contiguous United States. Part II: Supercell and QLCS tornado environments. *Wea. Forecasting*, **27**, 1136–1154, https://doi.org/10.1175/WAF-D-11-00116.1.

Wakimoto, R. M., and H. V. Murphey, 2009: Analysis of a dryline during IHOP: Implications for convection initiation. *Mon. Wea. Rev.*, **137**, 912–936, https://doi.org/10.1175/2008MWR2584.1.

Wasula, A. C., L. F. Bosart, and K. D. LaPenta, 2002: The influence of terrain on the severe weather distribution across interior eastern New York and western New England. *Wea. Forecasting*, **17**, 1277–1289, https://doi.org/10.1175/1520-0434(2002)017<1277:TIOTOT>2.0.CO;2.

Weckwerth, T. M., and D. B. Parsons, 2006: A review of convective initiation and motivation for IHOP_2002. *Mon. Wea. Rev.*, **134**, 5–22, https://doi.org/10.1175/MWR3067.1.

Whiteman, C. D., and J. C. Doran, 1993: The relationship between overlying synoptic-scale flows and winds within a valley. *J. Appl. Meteor.*, **32**, 1669–1682, https://doi.org/10.1175/1520-0450(1993)032<1669:TRBOSS>2.0.CO;2.

Wolf, P. L., 1998: WSR-88D radar depiction of supercell-bow echo interaction: Unexpected evolution of a large, tornadic, "comma-shaped" supercell over eastern Oklahoma. *Wea. Forecasting*, **13**, 492–504, https://doi.org/10.1175/1520-0434(1998)013<0492:WRDOSB>2.0.CO;2.

Xue, M., and W. J. Martin, 2006: A high-resolution modeling study of the 24 May 2002 dryline case during IHOP. Part II: Horizontal convective rolls and convective initiation. *Mon. Wea. Rev.*, **134**, 172–191, https://doi.org/10.1175/MWR3072.1.